



# Mach number and wall thermal boundary condition effects on near-wall compressible turbulence

Akanksha Baranwal<sup>1</sup> , Diego A. Donzis<sup>1</sup>  and Rodney D.W. Bowersox<sup>1</sup> 

<sup>1</sup>Department of Aerospace Engineering Texas A&M University, College Station, TX 77843, USA

Corresponding author: Akanksha Baranwal, [abaranwal03@tamu.edu](mailto:abaranwal03@tamu.edu)

(Received 6 July 2023; revised 7 November 2024; accepted 30 December 2024)

---

We investigate the effects of thermal boundary conditions and Mach number on turbulence close to walls. In particular, we study the near-wall asymptotic behaviour for adiabatic and pseudo-adiabatic walls, and compare to the asymptotic behaviour recently found near isothermal cold walls (Baranwal *et al.* 2022. *J. Fluid Mech.* **933**, A28). This is done by analysing a new large database of highly-resolved direct numerical simulations of turbulent channels with different wall thermal conditions and centreline Mach numbers. We observe that the asymptotic power-law behaviour of Reynolds stresses as well as heat fluxes does change with both centreline Mach number and thermal condition at the wall. Power-law exponents transition from their analytical expansion for solenoidal fields to those for non-solenoidal field as the Mach number is increased, though this transition is found to be dependent on the thermal boundary conditions. The correlation coefficients between velocity and temperature are also found to be affected by these factors. Consistent with recent proposals on universal behaviour of compressible turbulence, we find that dilatation at the wall is the key scaling parameter for these power-law exponents, providing a universal functional law that can provide a basis for general models of near-wall behaviour.

**Key words:** compressible boundary layers, turbulence simulation, supersonic flow

---

## 1. Introduction

The detailed dynamics of turbulence near the wall has first-order effects on phenomena such as heat transfer and viscous drag. When speeds are relatively low, many aspects of these flows are relatively well understood, such as scaling laws for mean quantities and Reynolds stresses. The situation is more challenging at higher speeds, where

© The Author(s), 2025. Published by Cambridge University Press. This is an Open Access article, distributed under the terms of the Creative Commons Attribution licence (<https://creativecommons.org/licenses/by/4.0/>), which permits unrestricted re-use, distribution and reproduction, provided the original article is properly cited.

compressibility effects become important and the physics more involved due to the interaction of hydrodynamics with thermodynamics. Understanding the detailed dynamics in such regimes is critical for accurate predictions and, ultimately, control of these flows. It is also critical for model development in the context of Reynolds-averaged Navier–Stokes (RANS) approaches, which are widely used in applications. Substantial efforts have been devoted to develop RANS models for compressible wall-bounded flows, with adiabatic and weakly cooled walls (Menter 1992; Spalart & Allmaras 1992; Catris & Aupoix 2000). However, these models result in poor prediction of statistics at high speeds (Roy & Blottner 2006; Rumsey 2010; Aiken *et al.* 2020) due to the lack of an accurate representation of the different physics and flow behaviour in different conditions. One important difference between different regimes is the wall thermal boundary condition (WTBC) which, in general, is modelled as adiabatic at supersonic speeds but cold-wall isothermal in hypersonic regimes. In certain situations, it is also possible to have mixed boundary conditions, which can again alter the flow dynamics.

Direct numerical simulations (DNS) of a number of wall-bounded flows, such as channels (Coleman *et al.* 1995; Huang *et al.* 1995; Foyi *et al.* 2004; Morinishi *et al.* 2004; Gerolymos & Vallet 2014; Sciacovelli *et al.* 2017; Yu *et al.* 2019; Yao & Hussain 2020) and flat-plate boundary layers (Smits & Dussauge 2006; Wenzel *et al.* 2018; and references therein) have been conducted to try to understand compressibility effects on turbulence statistics in high-speed regimes. Efforts have also been made to study the effects of the WTBC on the scaling of velocity and temperature statistics, and the relationship between them in high-speed regimes (Huang *et al.* 1995; Morinishi *et al.* 2004; Mader 2000; Tamano & Morinishi 2006; Duan *et al.* 2010; Shadloo *et al.* 2015; Hadjadj *et al.* 2015; Shahab *et al.* 2011; Zhang *et al.* 2014, 2018, 2022a). Recent studies have investigated the effects of thermal wall condition on pressure fluctuations (Zhang *et al.* 2017, 2022b), kinetic energy transfer (Xu *et al.* 2021b), density and temperature resolvent mode shapes (Bae *et al.* 2020) highlighting WTBC effects on turbulent processes and structures. Several studies focused on finding scaling laws, and others on using these scaling laws to collapse first- and second-order statistics in high-speed regimes for different flow conditions and different WTBCs (Brun *et al.* 2008; Zhang *et al.* 2012; Patel *et al.* 2015; Trettel & Larsson 2016; Volpiani *et al.* 2020; Griffin *et al.* 2021). For example, a recent study by Cogo *et al.* (2022) demonstrated excellent collapse of mean velocity profiles using recent transformations proposed by Volpiani *et al.* (2020) and Griffin *et al.* (2021) for high-speed zero-pressure-gradient turbulent boundary layers up to friction Reynolds number  $\approx 2000$ . Other recent studies have focused on studying the effects of Mach number and WTBCs on near-wall turbulence behaviour by quantifying their effects with new proposed parameters. Wenzel *et al.* (2022) proposed the Eckert number, which seems to be able to accommodate wall-cooling effects at different Mach numbers. Cogo *et al.* (2022, 2023) demonstrated that variations in the WTBC or/and Mach number significantly impact the near-wall velocity and temperature correlations. These WTBCs can be broadly characterized as isothermal (constant temperature) and isoflux (constant heat flux) conditions. For the former, studies have been conducted to investigate the effect of wall temperature, and for the latter, the effect of varying rate of heat transfer. Some studies have also used the so-called pseudo-adiabatic wall, a constant wall temperature (based on the recovery factor) whose value is such that the mean heat transfer to the wall vanishes, mimicking an adiabatic boundary. Some of the studies mentioned above (Shadloo *et al.* 2015; Wenzel *et al.* 2018; Zhang *et al.* 2022a) found that variations in turbulence statistics (e.g. mean velocity, mean temperature, Reynolds stresses) are due not to changes in the WTBC itself (i.e. change from isothermal to isoflux), but instead to change in the heat transfer at the wall. However, direct effects of changing the boundary condition from isothermal to isoflux were observed on temperature

fluctuation statistics (e.g. temperature fluxes in the near-wall region), and these effects extended beyond the viscous sublayer. Another important observation was the change in asymptotic behaviour of turbulent heat fluxes for different WTBCs.

From a fundamental and modelling perspective, it is crucial to understand the precise asymptotic behaviour of turbulence close to the wall. Indeed, accurate prediction necessitates models to satisfy the correct asymptotic scaling laws (Lai & So 1990; Germano *et al.* 1991; So *et al.* 1991*a,b*, 1998; Zhang *et al.* 1992; Durbin 1993; Sommer *et al.* 1993; Bowersox 2009; Agrawal *et al.* 2022), thus many studies have reported the asymptotic behaviour of turbulent fluxes for both incompressible and compressible flows, and under different WTBCs (Morinishi *et al.* 2004; Li *et al.* 2009; Shadloo *et al.* 2015; Hadjadj *et al.* 2015; Zhang *et al.* 2022*a*). All these studies compared their data to the theoretical asymptotes obtained from Taylor series expansions in the wall-normal direction, and found good agreement. However, none of these studies examined well-resolved wall asymptotes with a systematic variation of Mach number for different WTBCs.

We have recently conducted DNS of turbulent channels with finer near-wall resolution than the standard in the literature to capture true asymptotic behaviour (Baranwal *et al.* 2022). In that study, which was done with cooled isothermal walls, we systematically varied the centreline Mach number from  $M \gtrsim 0.2$  (virtually incompressible) to  $M \lesssim 2.2$ . We showed that turbulent stresses and wall-normal heat flux comprising at least one wall-normal velocity component do not collapse when the Mach number is changed, as suggested by widely used scaling laws, which thus undermines Morkovin's hypothesis. In particular, due to the extremely high wall resolution, we were able to unveil a new region very close to the wall where power-law scaling exponents were found to differ from theoretical asymptotes, and furthermore, depend on Mach number. Previous studies at the standard resolution are not able to capture this region. We have also found that increasing the centreline Mach number resulted in enhanced levels of dilatation motions at the wall, which is the key factor to understand changes in the power-law asymptotes close to the wall. Dilatational levels at the wall were also found to be affected by WTBCs in boundary layers (Xu *et al.* 2021*b*; Zhang *et al.* 2022*b*). Zhang *et al.* (2022*b*) further found that wall cooling effects on dilatation depend also on the Mach number.

These complex dependencies on both WTBCs and Mach number are the motivation behind the present work. In particular, we investigate, for the first time, the asymptotic behaviour of various turbulent stresses and heat fluxes at different Mach numbers and for different WTBCs. This systematic investigation is possible due to extremely well resolved turbulent channels with centreline Mach number ranging from 0.2 to 2.2, with isothermal, adiabatic and pseudo-adiabatic walls. The new adiabatic and pseudo-adiabatic results complement the isothermal data in Baranwal *et al.* (2022). This is also relevant in the context of classical scaling laws based on Morkovin's hypothesis, which are more effective at collapsing statistics when the walls are adiabatic or weakly cooled than when they are isothermal, in which case there is significant wall cooling. Adiabatic walls thus possess the additional advantage of isolating the effects of Mach number from wall cooling, and provide a more direct way to assess the effects of Mach number in isolation, and the validity of Morkovin's hypothesis on the asymptotic scaling of turbulence statistics.

The rest of the paper is organized as follows. We first present the numerical method, configuration and DNS database. Then we present results on the asymptotic behaviour of Reynolds stresses and their dependency on centreline Mach number and WTBCs. This analysis is then extended to temperature fluctuations and heat fluxes. We complement the analysis with a discussion based on visualizations of fluctuating quantities close to the wall, which allows us to infer some important correlations to explain the universal

| Wall             | $M_c$ | $Re_c$ | $Re_\tau$ | $Re_\tau^*$ | $\Delta y_{min}^+$ | $\Delta y_{max}^+$ | $\Delta x^+$ | $\Delta z^+$ | Line style |
|------------------|-------|--------|-----------|-------------|--------------------|--------------------|--------------|--------------|------------|
| Isothermal       | 0.23  | 5692   | 295       | 293         | 0.08               | 2.9                | 14.5         | 4.8          | —          |
| Adiabatic        | 0.23  | 5684   | 296       | 292         | 0.08               | 2.9                | 14.5         | 4.8          | - - - -    |
| Isothermal       | 0.35  | 5638   | 294       | 289         | 0.08               | 2.9                | 14.4         | 4.8          | —          |
| Isothermal       | 0.46  | 5582   | 294       | 286         | 0.08               | 2.9                | 14.4         | 4.8          | —          |
| Isothermal       | 0.57  | 5476   | 293       | 281         | 0.05               | 3.2                | 14.4         | 4.8          | —          |
| Adiabatic        | 0.57  | 5476   | 293       | 281         | 0.05               | 3.2                | 14.4         | 4.8          | - - - -    |
| Isothermal       | 0.68  | 5498   | 301       | 283         | 0.05               | 3.3                | 14.8         | 4.9          | —          |
| Isothermal       | 0.89  | 5371   | 307       | 276         | 0.05               | 3.4                | 15.1         | 5.0          | —          |
| Adiabatic        | 0.84  | 5099   | 225       | 260         | 0.05               | 2.2                | 11.0         | 3.6          | - - - -    |
| Isothermal       | 1.26  | 5022   | 325       | 259         | 0.05               | 3.6                | 15.9         | 5.3          | —          |
| Adiabatic        | 1.12  | 4513   | 177       | 226         | 0.05               | 1.7                | 8.7          | 2.9          | - - - -    |
| Pseudo-adiabatic | 1.12  | 4306   | 179       | 220         | 0.05               | 1.7                | 8.8          | 2.9          | - - - -    |
| Isothermal       | 1.50  | 5489   | 393       | 277         | 0.10               | 4.0                | 19.3         | 6.4          | —          |
| Isothermal       | 1.98  | 5631   | 572       | 279         | 0.10               | 6.2                | 14.0         | 4.7          | —          |
| Adiabatic        | 1.9   | 5092   | 138       | 236         | 0.05               | 1.0                | 3.4          | 1.0          | - - - -    |
| Isothermal       | 2.22  | 5666   | 745       | 273         | 0.09               | 8.8                | 14.8         | 6.1          | —          |

Table 1. Details of flow conditions and grid resolutions.

behaviour put forth here. We conclude with a summary and some remarks on the implications of the results presented here.

## 2. Numerical method

We perform DNS of the equations governing mass, momentum and energy conservation for a compressible channel flow. The equations are discretized on a uniform mesh in the streamwise ( $x$ ) and spanwise ( $z$ ) directions. In the wall-normal ( $y$ ) direction, the grid is clustered close to the wall using a hyperbolic tangent function. We use sixth-order compact schemes to compute spatial derivatives in the  $x$  and  $z$  directions. For the  $y$  direction, we utilize the sixth-order compact scheme in interior points, and the order is reduced to fourth and third at the last two grid points in the domain. The variables are marched in time using a third-order low-storage Runge–Kutta scheme. More details on simulations can be found in our recent studies on compressible channels (Baranwal *et al.* 2022; Baranwal 2023), where we also present detailed grid convergence studies and validations against other DNS databases in the literature (e.g. Coleman *et al.* 1995). The simulations presented here satisfy the resolution criteria that are summarized in table 1.

The molecular viscosity  $\mu$  obeys a power law of the form  $T^a$ , where  $a = 0.5$ . Other values have been used in the literature in the range 0.5–0.75. Recent results, however, appear to indicate that many statistics are robust to these changes, especially those related to self-similar behaviour (John & Donzis 2024). The thermal conductivity  $\kappa$  is related to  $\mu$  through  $\kappa = \mu C_p / Pr$ , with Prandtl number  $Pr = 0.7$ . To close the system of equations, the ideal gas equation of state is assumed.

For our low Mach number case, velocity and temperature profiles are initialized with an incompressible laminar profile with random velocity fluctuations with zero mean. The temperature and density fluctuations are initialized to be zero. Density is kept constant across the channel and is equal to its bulk value. Simulations are evolved until a steady state is reached, after which statistics are collected. Simulations with higher Mach numbers are initialized from scaling the profile resulting from a lower Mach number such that the initial profiles match the desired mass flow rates.

Periodic boundary conditions are used in the streamwise and spanwise directions. At the walls, we apply no-slip boundary conditions for all velocity components. The boundary condition for pressure is obtained by evaluating the momentum equation in the normal direction at the wall, which was found to have a greater numerical stability than the commonly used zero-pressure gradient (Baranwal *et al.* 2022). Three additional elements have been used to ensure the stability of the numerical approach. First, we use a Courant–Friedrichs–Lewy (CFL) number in the range 0.2–0.4, which was found to eliminate spurious fluctuations that were occasionally observed at different distances from the wall at different conditions. Second, we use a finer-than-usual resolution in the wall-normal direction to resolve the asymptotic region at the wall. Finally, the nonlinear terms are discretized using a skew-symmetric formulation that has been shown to provide robust stability characteristics (Blaisdell *et al.* 1996; Jagannathan & Donzis 2016).

In all the simulations presented here, the bottom wall ( $y = 0$ ) is isothermal with  $T = T_0$ . For the top wall, three different thermal boundary conditions are investigated, namely, isothermal, adiabatic and pseudo-adiabatic cases, denoted by I, A and PA respectively. For isothermal cases, the top wall is kept at the same temperature as the bottom wall ( $T_0$ ). These simulations, which were studied in our previous study (Baranwal *et al.* 2022), act as base case to compare with other thermal wall conditions. For adiabatic cases, we specify zero temperature gradient at the top wall. This approach with mixed boundary conditions in a channel has been used before (Morinishi *et al.* 2004; Tamano & Morinishi 2006; Zhang *et al.* 2022a; Lusher & Coleman 2022; Baranwal *et al.* 2023). Finally, the pseudo-adiabatic case consists of imposing an isothermal boundary condition at the average temperature obtained from the adiabatic simulation with all other flow parameters kept the same as in the adiabatic case.

Following standard notation, the bulk, wall and centreline values of a variable  $f$  are denoted by  $f_b$ ,  $f_w$  and  $f_c$ , respectively. Reynolds and Favre decompositions are denoted by  $\bar{q} + q'$  and  $\tilde{q} + q''$ , respectively. The averages in these decompositions are taken along the homogeneous directions (i.e.  $x$ – $z$  planes) and time. As done in Baranwal *et al.* (2022), snapshots of all fields are saved at time intervals of  $5h/\bar{u}_b$  for all simulations, where  $h$  is the channel half-width, and  $u$  is the streamwise velocity component. This time scale ( $h/\bar{u}_b$ ) is commensurate with the eddy-turnover time of the turbulence in the centre of the channel, thus representative of the largest turbulent structures. Our temporal averages involved 25 snapshots for velocity, density and temperature fields.

Consider a forced, periodic channel with Dirichlet boundary conditions for temperature at the walls, i.e. isothermal walls. If initialized with zero velocity and constant temperature, the flow will accelerate and develop velocity gradients that lead to viscous dissipation. This leads to an increase in temperature inside the channel that is higher than that imposed at the walls. Because of the thermal gradient that forms at the wall, there is a flux of energy from the fluid to the wall, and the flow eventually reaches a statistically steady state where the rate of production of internal energy due to viscous dissipation is compensated by the energy transfer through the wall. If, on the other hand, we apply a Neumann boundary condition for temperature at the wall, in particular zero temperature gradient, then the heat transfer to the walls is identically zero. In this case, the increase in temperature due to dissipation maintained by the forcing in the momentum equation is not balanced by heat flux through the walls. Therefore, the internal energy in the channel increases continuously, leading to a time-dependent mean thermodynamic state. Alternatively, one can apply a (cold) isothermal condition to one wall and an adiabatic condition to the other wall. This allows for heat transfer through one wall, and results in a decreased rate of change of mean thermodynamic parameters. In this case, the flow also achieves a pseudo-steady state where statistics (at least to second order) are in a statistically steady state when

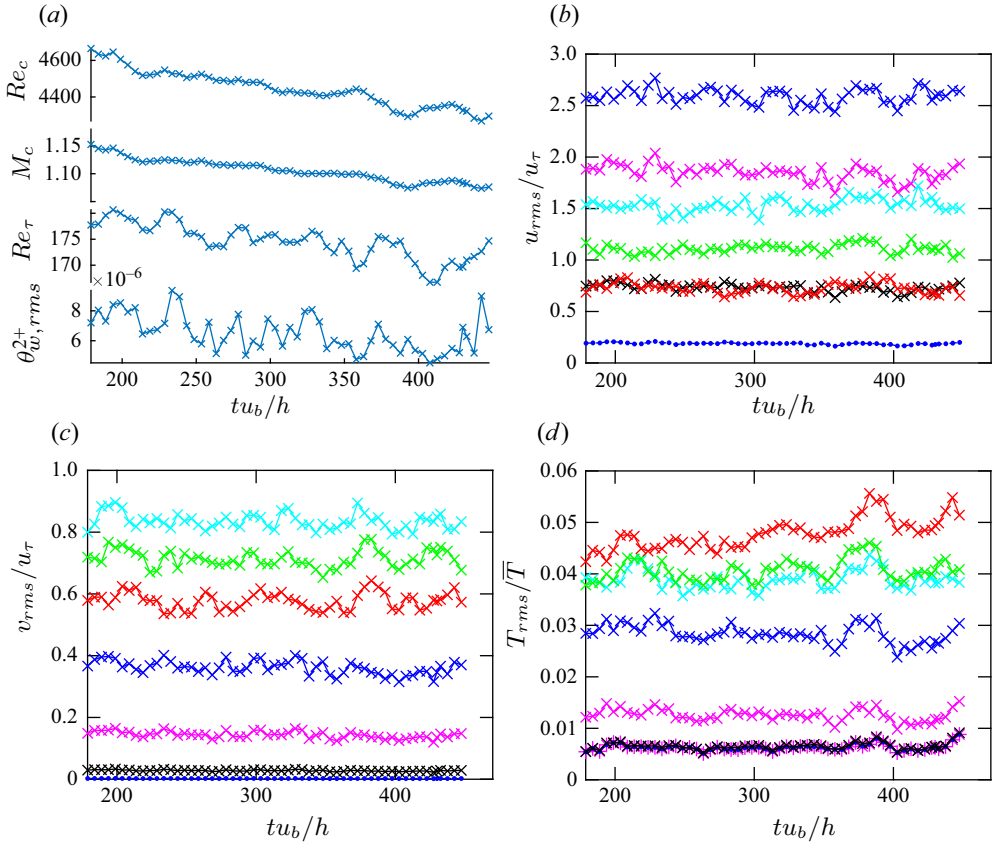


Figure 1. Time evolution of (a)  $Re_c$ ,  $M_c$ ,  $Re_\tau$ ,  $\theta_{w,rms}^{+2}$ , (b)  $u_{rms}/u_\tau$ , (c)  $v_{rms}/u_\tau$ , (d)  $T_{rms}/\bar{T}$ , for  $M_b \approx 1.2$ . Magenta \* indicate  $y^+ = 0$ ; blue dots indicate  $y^+ = 0.5$ . Symbols  $\times$  are black for  $y^+ = 2.0$ , magenta for  $y^+ = 5.6$ , dark blue for  $y^+ = 11$ , light blue for  $y^+ = 54$ , green for  $y^+ = 100$ , and red for  $y^+ = 173$ .

normalized by their corresponding (slowly varying) means. This can be seen in figures 1(b–d), where we show the temporal evolution of the root mean square (r.m.s.) of several variables normalized by their respective time-varying means for  $M_b \approx 1.2$  and very long simulation time ( $\approx 200h/u_b$ ). While global quantities (Reynolds and Mach numbers in figure 1a) are seen to decrease slowly, normalized fluctuations statistics are virtually in a statistical steady state. This is, in fact, consistent with observation in forced isotropic flows (Kida & Orszag 1990). We do note that there seems to be a (very weak) increase in  $T_{rms}$  at the centreline ( $y^+ = 173$ , red symbols). Because our interest lies close to the wall, we have verified that this trend very far from the wall is not a concern in this study.

The normalized r.m.s. dilatation at the wall  $\theta_{w,rms}^+ = \left[ \overline{(\partial v'/\partial y)^2 v_w^2 / u_\tau^4} \right]^{1/2}$ , as shown in figure 1(a), is another quantity of interest that also exhibits a steady-state behaviour. We take advantage of this pseudo-steady state to find averages over the simulation time. The statistics below are based on this averaging.

The friction Reynolds numbers based on wall quantities, and the friction Reynolds numbers based on centreline viscosity and density, are defined as  $Re_\tau = \bar{\rho}_w u_\tau h / \bar{\mu}_w$  and  $Re_\tau^* \equiv \bar{\rho}_c (\tau_w / \bar{\rho}_c)^{1/2} h / \bar{\mu}_c$ , respectively, with  $u_\tau \equiv \sqrt{\tau_w / \bar{\rho}_w}$  being the friction velocity. The centreline Reynolds number and centreline Mach numbers are  $Re_c \equiv \bar{\rho}_c \bar{u}_c h / \bar{\mu}_c$  and

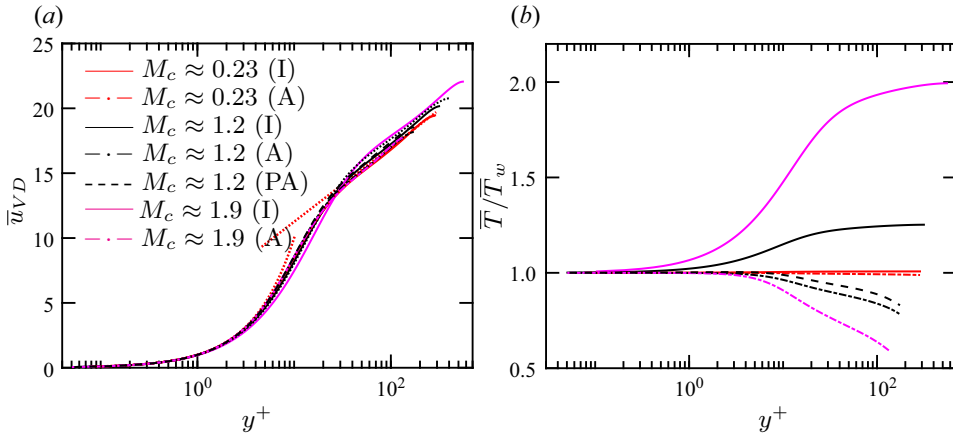


Figure 2. (a) The Van Driest transformed streamwise mean velocity. (b) Mean temperature normalized by the mean wall temperature plotted against the wall-normal coordinate in viscous units for isothermal (solid line), adiabatic (dash-dotted line) and pseudo-adiabatic (dashed line) cases. Red, black and magenta correspond to  $M_c \approx 0.23$ ,  $M_c \approx 1.2$  and  $M_c \approx 1.9$ , respectively. Dotted red lines represent viscous and log layer scalings.

$M_c \equiv \bar{u}_c / \sqrt{\gamma R \bar{T}_c}$ , respectively. Our domain has dimensions  $4\pi h \times 2h \times 4\pi/3h$  for all our simulations. This is larger than widely used in the literature (e.g. Trettel & Larsson 2016; Yu *et al.* 2019). Finally, as a direct assessment of boundary conditions effects on the quantities studied here, we have run additional simulations with a domain that is 20 % shorter, and confirmed that the near-wall scaling laws are unaffected. Table 1 summarizes the important parameters for the DNS database used here.

In subsequent sections, we investigate various statistics near isothermal (solid lines) and adiabatic (dash-dotted lines) walls for three different centreline Mach numbers,  $M_c \approx 0.23$  (red),  $M_c \approx 1.2$  (black) and  $M_c \approx 1.9$  (magenta), and near pseudo-adiabatic walls (dashed lines) for  $M_c \approx 1.2$  using our DNS database. The adiabatic and pseudo-adiabatic results are taken from the upper halves of the channel from the A and PA simulations, respectively, where bottom walls are isothermal. The isothermal case throughout the work refers to simulations where both walls are isothermal, unless specifically noted otherwise. We note that wall quantities for a particular case refer to the statistics at the wall with that particular thermal boundary condition (e.g. for the pseudo-adiabatic case, wall quantities refer to statistics at the pseudo-adiabatic wall).

### 3. First-order statistics

The Van Driest transformed velocity (Van Driest 1951) and the mean temperature normalized by the wall temperature are shown in figures 2(a,b), respectively. Consistent with the literature, Van Driest transformation ( $u_\tau$ ) performs well in collapsing velocity, except at  $M_c \approx 1.9$  with isothermal walls where a slight deviation from the low Mach velocity profile can be observed. This is consistent with several recent studies (Brun *et al.* 2008; Zhang *et al.* 2012; Trettel & Larsson 2016; Patel *et al.* 2015; Volpiani *et al.* 2020; Griffin *et al.* 2021) that have proposed various transformations to collapse mean velocity profiles in compressible wall-bounded flows; readers are referred to these studies for details and applicability of these transformations.

In figure 2(b), consistent with the literature (Huang *et al.* 1995; Morinishi *et al.* 2004), we observe that for isothermal cases, wall cooling leads to a temperature inside the

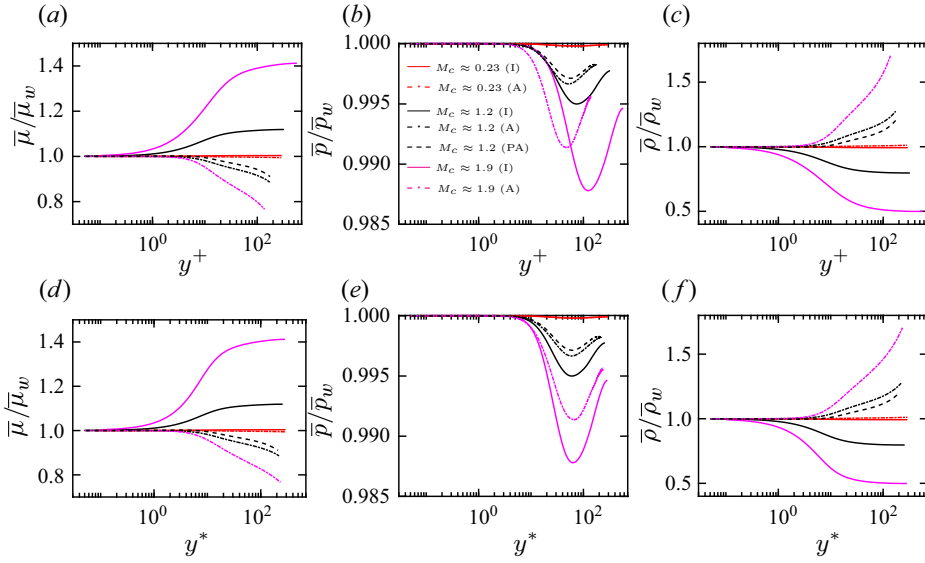


Figure 3. Mean (a,d) viscosity, (b,e) pressure and (c,f) density, normalized by their corresponding wall values and plotted versus wall-normal coordinate in (a–c) viscous units and (d–f) semi-local units, for isothermal (solid line), adiabatic (dash-dotted line) and pseudo-adiabatic (dashed line) cases. Red, black and magenta correspond to  $M_c \approx 0.23$ ,  $M_c \approx 1.2$  and  $M_c \approx 1.9$ , respectively.

channel that is higher than the wall temperature, with a maximum at the centreline. This maximum temperature along with the wall cooling rate increases with the Mach number. For adiabatic cases, because of the zero heat flux at the top wall, there is a rise of temperature across the channel, with the maximum temperature at the upper wall. The temperature gradient for adiabatic and pseudo-adiabatic cases is not zero at the centreline, which may result in non-zero temperature fluxes at the channel half-width, an effect that will be discussed later.

The mean viscosity, mean pressure and mean density are shown in figure 3 against wall-normalized (figures 3a–c) and semi-local (figures 3d–f) wall-normal coordinates. On comparing figures 3(a) and 3(d), figures 3(b) and 3(e), and figures 3(c) and 3(f), we observe that some features become independent of Mach number or WTBC when the statistics are plotted against the semi-local wall-normal coordinate  $y^* \equiv \bar{\rho}(\tau_w/\bar{\rho})^{1/2}y/\bar{\mu}$  as opposed to  $y^+$ . For example, in figure 3(e), we see that pressure starts decreasing significantly only at  $y^* \approx 5$ , reaching a minimum at  $y^* \approx 65$  for all  $M_c$ , and then increasing towards the channel centreline. Similar observations can be made for viscosity and density for isothermal cases (figures 3d,f). As expected, the mean viscosity follows a trend similar to that of the mean temperature (figure 2b). Pressure is relatively constant across the channel, with a small dip outside the viscous sublayer that increases with  $M_c$  to approximately 1.5% at the highest Mach number shown ( $M_c \approx 1.9$ ). In figures 3(c) and 3(f), we show the mean density normalized by the mean density at the wall. Because the mean pressure is approximately constant across the channel, the mean density is inversely proportional to the mean temperature, which is what we observe in these plots.

We can also see opposite trends depending on the WTBC. For isothermal cases, the density decreases as one moves away from the wall or when the Mach number increases. For adiabatic and pseudo-adiabatic cases, on the other hand, the density increases as one moves away from the wall or when the Mach number decreases. A result of these trends is

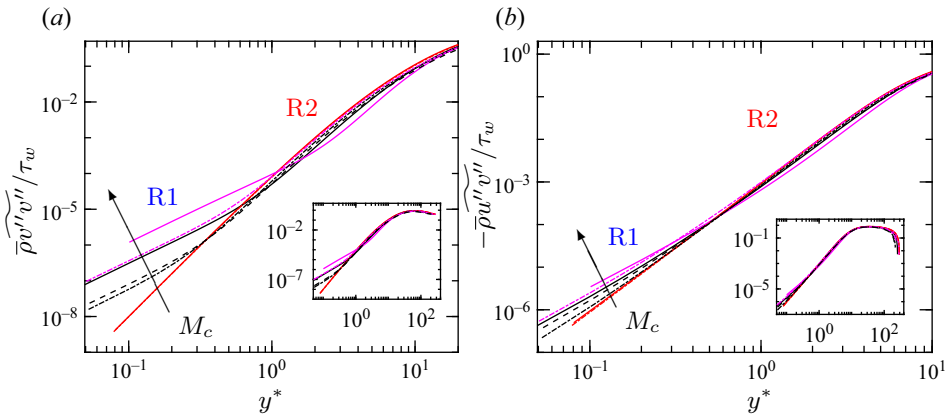


Figure 4. Density-scaled Reynolds stresses distributions versus semi-local wall-normal coordinate for isothermal (solid line), adiabatic (dash-dotted line) and pseudo-adiabatic (dashed line) cases. Red, black and magenta correspond to  $M_c \approx 0.23$ ,  $M_c \approx 1.2$  and  $M_c \approx 1.9$ , respectively. Insets show the same profiles up to  $y^* \approx 300$ .

that close to the wall, the density gradients are higher for isothermal cases at higher Mach numbers, indicating that the statistics will change more rapidly from their wall values in the near-wall region when the level of compressibility and heat transfer to the wall are increased.

#### 4. Effects of thermal boundary conditions on turbulent stresses

The wall-normal coordinate in semi-local units  $y^*$  along with local density-weighted averaging have been widely used to try to collapse turbulent stresses in compressible wall-bounded flow with varying WTBCs, with their incompressible counterparts (Huang *et al.* 1995; Foyi *et al.* 2004; Morinishi *et al.* 2004; Trettel & Larsson 2016; Modesti & Pirozzoli 2016; Zhang *et al.* 2018). We have shown recently (Baranwal *et al.* 2022), however, that semi-local scaling is not able to collapse turbulent stresses  $R_{\alpha\beta}^* \equiv \overline{\rho \alpha'' \beta''} / \tau_w$  (where  $\alpha$  and  $\beta$  are velocity components, e.g.  $R_{uv}^* \equiv \overline{\rho u'' v''} / \tau_w$ ) or the wall-normal turbulent heat flux  $R_{vT}^* = \overline{\rho v'' T''} / (\rho_w u_\tau T_\tau)$  close to an isothermal wall in turbulent channels for centreline Mach numbers ranging from the incompressible limit to supersonic regimes. This can also be observed here in e.g. figures 4(a,b).

In figure 4, we show  $R_{vv}^*$  and  $R_{uv}^*$ , respectively, for three Mach numbers,  $M_c \approx 0.23$ , 1.2, 1.9, for both isothermal (solid line) and adiabatic (dash-dotted line) walls. The figure also includes one pseudo-adiabatic case (dashed line) at  $M_c \approx 1.2$ . At the lowest Mach number ( $M_c \approx 0.23$ ), turbulent stresses ( $R_{vv}^*$ ,  $R_{uv}^*$ ) collapse well for isothermal and adiabatic walls, suggesting no appreciable WTBC effect as one approaches the incompressible limit. As the Mach number is increased, however, we can clearly observe differences between isothermal, adiabatic and pseudo-adiabatic cases for  $R_{vv}^*$ , which are apparent for  $M_c \approx 1.2$  and beyond. Though smaller,  $R_{uv}^*$  also show some differences in R1. This effect is especially strong in the viscous sublayer, where we can clearly see higher normal Reynolds stresses close to isothermal (solid line) than to adiabatic (dashed-dotted line) walls. However, one can also observe that some Mach number effects are similar in isothermal cases and adiabatic cases. Investigating these differences and similarities is the main focus of the current work.

|                | $\overline{v'v'}$ | $\overline{u'v'}$ |            | $\overline{v'T'}$ |                  |
|----------------|-------------------|-------------------|------------|-------------------|------------------|
|                |                   |                   | Isothermal | Adiabatic         | Pseudo-adiabatic |
| Solenoidal     | 4                 | 3                 | 3          | 2                 | 3                |
| Non-solenoidal | 2                 | 2                 | 2          | 1                 | 2                |

Table 2. Exponents  $\gamma_{\alpha\beta}$  for near-wall asymptotic behaviour for  $R_{\alpha\beta}$  (where  $\alpha$  and  $\beta$  are  $u, v$  or  $T$ ).

Three observations can be made. First, in the region adjacent to the wall, indicated by R1 in figure 4, we can see power-law behaviour for both  $R_{uv}^*$  and  $R_{vv}^*$ , with exponents that decrease with  $M_c$  for adiabatic cases and, as observed before, isothermal cases (Baranwal *et al.* 2022). The slope of  $R_{uv}^*$  in R1, however, does change with the WTBC when  $M_c$  is kept constant. This WTBC effect is weaker for  $R_{vv}^*$ . Second,  $R_{uv}^*$  and  $R_{vv}^*$  transition to another scaling regime, indicated as R2 in figure 4, with much weaker WTBC and  $M_c$  effects. Consistent with the analytical analysis, it will shortly be shown that the change in value of power-law exponents from R1 to R2 for  $R_{vv}$  is higher than that for  $R_{uv}$ . The differences observed here for  $R_{uv}$  will become more apparent when this quantitative analysis is done for the power-law asymptotes. Finally, the transition location changes with both  $M_c$  and WTBC. Taken together, these general observations suggest that significant WTBC and Mach number effects are observed close to the wall as Mach number increases.

The near-wall asymptotic behaviour of turbulent stresses can be estimated theoretically by expanding the constituent velocity components as Taylor series expansions in  $y$ :

$$u' = a_u + b_u y + c_u y^2 + \dots, \quad v' = a_v + b_v y + c_v y^2 + \dots \quad (4.1)$$

The coefficients  $a_\alpha$  for  $\alpha = u, v$  are identically zero due to the no-slip boundary condition at the wall. The other coefficients are given by  $b_v = \partial v' / \partial y$  and  $c_v = (1/2) \partial^2 v' / \partial y^2$ , and similarly for  $u$ . If the flow is incompressible (solenoidal), then mass conservation combined with the no-slip condition at the wall leads to an additional constraint in the wall-normal velocity component, namely,  $\partial v' / \partial y = b_v = 0$ . On the other hand, if the flow is non-solenoidal, then  $b_v \neq 0$ . By taking the product of the expansions of different components and averaging, one can formulate Reynolds-averaged turbulent stresses ( $R_{\alpha\beta} \equiv \overline{\alpha' \beta'} / u_\tau^2$ ), resulting in near-wall scaling laws of the form  $R_{\alpha\beta} \approx \sigma_{\alpha\beta} y^{\gamma_{\alpha\beta}}$ , with exponents summarized in table 2. These theoretical exponents are the same for  $R_{\alpha\beta}$  and  $R_{\alpha\beta}^*$  given that density has a finite value at the wall. From table 2, we see that the solenoidal and non-solenoidal exponents are different for turbulent stresses containing a wall-normal velocity component. As in Baranwal *et al.* (2022), we investigate exponents ( $\gamma_{\alpha\beta}$ ) and prefactors ( $\sigma_{\alpha\beta}$ ), but extend the analysis to include WTBC effects.

We also note that the expansion in  $y^+$  is identical to  $y$  in terms of exponents since the normalizing variables in  $y^+$  are independent of  $y$ . When  $y^*$  is plotted against  $y^+$  (not shown here), we see that in R1, the difference between  $y^*$  and  $y^+$  is, as expected, negligible since local values of density and viscosity are not far from those at the wall. Because  $y^+$  has the same expansion as  $y$ ,  $y^*$  is also well approximated by this expansion in R1. Put more formally, one can incorporate density and viscosity in the expansion for which the corresponding variations will be, respectively,  $\rho \approx \rho_w + a_\rho y + \dots$  and  $\mu \approx \mu_w + a_\mu y + \dots$ . If these are incorporated in the analysis, then one would find that the asymptotic behaviour at the wall will not change since both  $\rho$  and  $\mu$  are constant to the lowest order.

Following Baranwal *et al.* (2022), we fit power laws in regions R1 and R2, as shown in figure 4 for both wall ( $R_{\alpha\beta}$  versus  $y^+$ , squares) and semi-local ( $R_{\alpha\beta}^*$  versus  $y^*$ ,

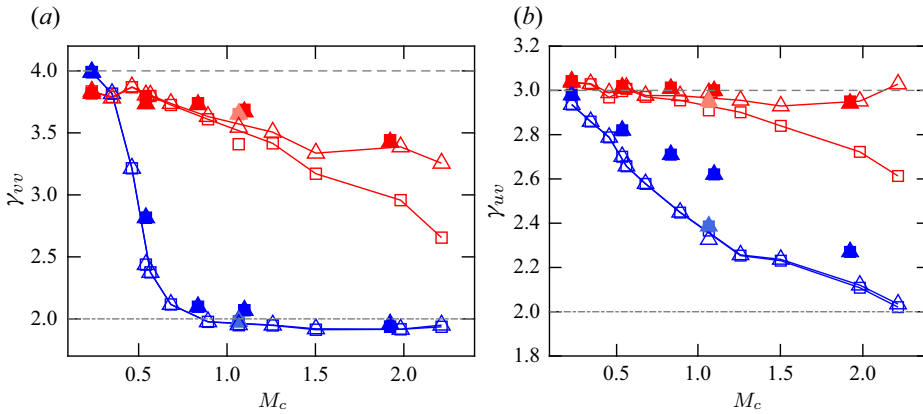


Figure 5. Power-law exponents for (a) wall-normal Reynolds stress, (b) Reynolds shear stress plotted against centreline Mach number. Horizontal grey lines indicate solenoidal (dashed) and non-solenoidal (dash-dotted) asymptotic exponents (table 2). Markers (see table 3): squares indicate wall normalizations ( $R_{\alpha\beta} = \sigma_{\alpha\beta}^+(y^+)^{\gamma_{\alpha\beta}^+}$ ), triangles indicate semi-local normalizations ( $R_{\alpha\beta}^* = \sigma_{\alpha\beta}^*(y^*)^{\gamma_{\alpha\beta}^*}$ ), for isothermal (empty markers), pseudo-adiabatic (light-filled markers) and adiabatic (dark-filled markers) cases. Blue and red markers correspond to R1 and R2 regions, respectively. The solid lines connect isothermal data for comparison.

|            | Isothermal |    | Adiabatic |    | Pseudo-adiabatic |    |
|------------|------------|----|-----------|----|------------------|----|
|            | R1         | R2 | R1        | R2 | R1               | R2 |
| Wall       | □          | □  | ■         | ■  | ■                | ■  |
| Semi-local | △          | △  | ▲         | ▲  | ▲                | ▲  |

Table 3. Marker styles used for exponents  $\gamma_{vv}$  and  $\gamma_{uv}$  for different WTBCs and scaling regimes.

triangles) normalizations, to obtain  $(\gamma_{\alpha\beta}^+, \sigma_{\alpha\beta}^+)$  and  $(\gamma_{\alpha\beta}^*, \sigma_{\alpha\beta}^*)$  respectively for all cases in our database. In figure 5(a), we show the exponent  $\gamma_{vv}$  for isothermal (empty markers), adiabatic (dark-filled markers) and pseudo-adiabatic (light-filled markers) wall conditions as functions of  $M_c$ . The theoretical asymptotic values in table 2 are expected to be attained for exponents in R1 (blue symbols) that are the closest to the wall. On changing thermal wall conditions, the difference between  $\gamma_{vv}$  in R1 is small for the same centreline Mach number except for  $M_c = 0.5$ , where the adiabatic case has a slightly larger exponent. The exponent  $\gamma_{vv}$  approaches its solenoidal and non-solenoidal limiting behaviour (see table 2) for  $M_c \lesssim 0.2$  and  $M_c \gtrsim 0.8$ , respectively. Between these two limits, there is a smooth transition with  $M_c$  for both isothermal and adiabatic cases.

In figure 5(b), we show the exponents for the shear Reynolds stress  $\gamma_{uv}$  versus  $M_c$ , and observe a much stronger influence of thermal boundary conditions with larger values of  $\gamma_{uv}$  in R1 for adiabatic cases at all Mach numbers. The pseudo-adiabatic case appears to match the isothermal case, which may not be completely unexpected given that in this case we also impose a constant temperature at the wall. This may indicate that  $\gamma_{uv}$  is independent of  $T_w$  since exponents for isothermal and pseudo-adiabatic are very close to each other even though wall temperature is markedly different. Furthermore, this may also suggest that differences in exponents for isothermal and adiabatic cases are not due to differences in wall temperature. The values obtained for the R1 exponents, however, are

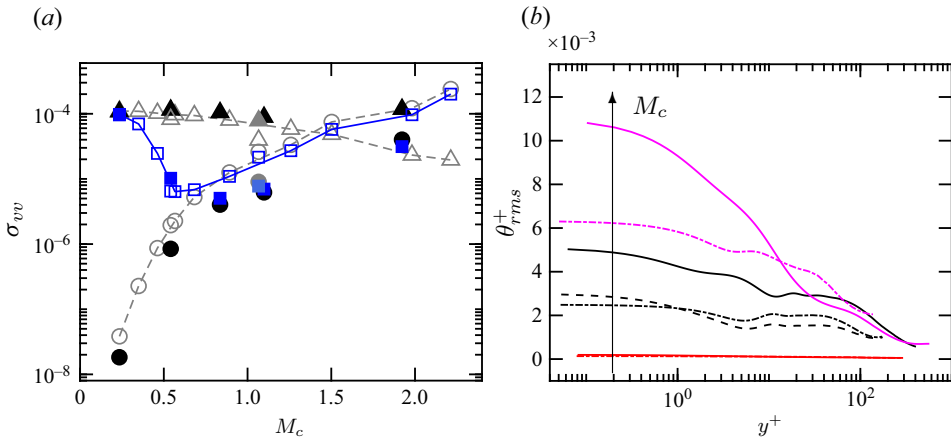


Figure 6. (a) Prefactor  $\sigma_{vv}$  (squares) in R1 and normalized coefficients in Taylor expansion for  $R_{vv}$ , non-solenoidal  $b_v^2 v_w^2 / u_\tau^4$  (circles) and solenoidal  $\bar{c}_v^2 v_w^4 / 4u_\tau^6$  (triangles) against  $M_c$  for different WTBCs. Markers are given in table 4. (b) Distribution of r.m.s. dilatation with wall-normal coordinate for isothermal (solid line), adiabatic (dash-dotted line) and pseudo-adiabatic (dashed line) cases. Red, black and magenta correspond to  $M_c \approx 0.23$ ,  $M_c \approx 1.2$  and  $M_c \approx 1.9$ , respectively.

independent of whether one uses wall or semi-local units for all WTBCs. This is in line with the theoretical behaviour discussed earlier.

In R2, semi-local normalization provides a better collapse of exponents with different WTBCs. This can be seen in figure 5(a), where we see that for a fixed  $M_c$ , there are negligible differences between  $\gamma_{vv}^*$  for isothermal (red empty triangles), adiabatic (red filled triangles) and pseudo-adiabatic (light red filled triangles) cases. Note also that  $\gamma_{vv}^+$  and  $\gamma_{vv}^*$  in R2 are the same for all Mach numbers for adiabatic cases, but not for isothermal cases. For isothermal cases, when  $M_c$  is approximately above unity,  $\gamma_{vv}^+$  and  $\gamma_{vv}^*$  differ. This can be understood by noting that the temperature and density gradients are higher near the isothermal wall than the adiabatic wall. Therefore, in adiabatic cases, local density and viscosity are closer to wall values as compared to those in isothermal cases (also seen in figures 3a–c). Similar behaviour is observed for  $\gamma_{uv}$ . In figure 4, we found that turbulent stresses in R2 are less affected by variations in Mach number when semi-local normalizations are used for different WTBCs. This is consistent with the results in figures 5(ab), where we see a very weak  $M_c$  effect on  $\gamma_{uv}^*$  (and to a lesser degree on  $\gamma_{vv}^*$ ) for all WTBCs. In general, though, we observe a weaker  $M_c$  dependence for adiabatic than isothermal walls for exponents in wall units.

In addition to obtaining exponents for isothermal cases from simulations where both walls are isothermal and at the same temperature, we also obtain the exponents close to the isothermal wall from simulations with different thermal boundary conditions (pseudo-adiabatic or adiabatic) on the other wall. In fact, the exponents  $\gamma_{vv}$  and  $\gamma_{uv}$  in R1 near the isothermal wall were found to be independent of the boundary condition of the other wall, indicating that the near-wall asymptotic behaviour is not significantly affected by the WTBC on the non-identical wall.

Written out explicitly, the first three terms in the expansion of the wall-normal Reynolds stress give  $\overline{v'v'} = b_v^2 y^2 + (\overline{b_v c_v} / 2) y^3 + (\overline{c_v^2} / 4 + \overline{b_v d_v} / 6) y^4 + \mathcal{O}(y^5)$ . As discussed above, when the flow is incompressible,  $b_v = 0$  and the  $y^4$  term dominates; when the flow is compressible, one expects the  $y^2$  term to dominate. However, this would also depend

|                                      | Isothermal | Adiabatic | Pseudo-adiabatic |
|--------------------------------------|------------|-----------|------------------|
| $\sigma_{vv}$                        | □          | ■         | ■                |
| $\overline{b_v^2} v_w^2 / u_\tau^4$  | ○          | ●         | ●                |
| $\overline{c_v^2} v_w^4 / 4u_\tau^6$ | △          | ▲         | ▲                |

Table 4. Marker styles used for prefactors and coefficients in Taylor series expansion for  $R_{vv}$  for different WTBCs.

on the prefactors involved,  $\overline{b_v^2}$  and  $\overline{c_v^2}$ , which in a particular region may make one term dominate the other. In figure 6(a), we show these prefactors normalized with wall units, i.e.  $\overline{b_v^2} v_w^2 / u_\tau^4 = \overline{(\partial v' / \partial y)^2} v_w^2 / u_\tau^4$  (circles) and  $\overline{c_v^2} v_w^4 / 4u_\tau^6 = \overline{(\partial^2 v' / \partial y^2)^2} v_w^4 / 4u_\tau^6$  (triangles) computed using the derivatives from DNS data at the wall. In the same plot, we also include the prefactor  $\sigma_{vv}^+$  obtained from the fits  $R_{vv} \approx \sigma_{vv}^+(y^+) \gamma_{vv}^+$  as described above. We can clearly see that  $\sigma_{vv}^+$  (squares) tends to the solenoidal (triangles) and non-solenoidal (circles) analytical values for  $M_c \lesssim 0.2$  and  $M_c \gtrsim 0.8$ , respectively, for isothermal (empty markers) and adiabatic (dark-filled markers) wall conditions. The pseudo-adiabatic (light-filled markers) case with  $M_c \approx 1.2$  also follows the analytical non-solenoidal value. These observations are consistent with the behaviour of exponents obtained from the fit. The value of  $\sigma_{vv}^+$  (squares) is also found to be lower for adiabatic (dark-filled) than isothermal (empty) cases at  $M_c \gtrsim 0.8$ . We finally note that at high Mach numbers, the dominant prefactor is the one involving  $b_v$ , which for no-slip walls is equal to the level of dilatation motions at the wall (Baranwal *et al.* 2022). Thus from a purely kinematic standpoint, the particular scaling laws observed will depend only on dilatation (i.e.  $b_v$ ) regardless of how those dilatations are generated.

It is known that different levels of dilatation at the wall can be generated by changing either the centreline Mach number (Baranwal *et al.* 2022) or the thermal boundary condition at the wall (Xu *et al.* (2021b)). This is also clear in figure 6(b), where we observe that the level of dilatational motions at the wall is different for different Mach numbers and WTBCs. Dilatation levels are weaker for adiabatic than isothermal walls with the same  $M_c$ . Pseudo-adiabatic walls have intermediate dilatation levels close to the wall. As stated previously, dilatation is a key factor governing the scaling laws, and one may thus expect better collapse of different statistics when using the dilatational content as a normalizing parameter. This general concept of universality based on the level of dilatational motions independent of the specific mechanism that generated them was indeed proposed recently (Donzis & Panickacheril 2020), though only for homogeneous flows.

To test these concepts, in figures 7(ab) we show the exponents as a function of the r.m.s. of dilatation at the wall normalized with wall units,  $\theta_{w,rms}^+$ . We clearly see a better collapse of exponents than in the corresponding plots of figures 5(a,b), supporting the idea that dilatational levels, regardless of how they are generated, provide the appropriate scaling parameter for near-wall behaviour at high speeds. This is consistent with Donzis & Panickacheril (2020), where the use of dilatational content as a governing parameter yielded a universal behaviour for a number of statistics, including pressure variance, dissipation, and skewness of the velocity gradients. From a modelling perspective, it may be useful to parametrize these seemingly universal curves. We have found that these curves can be represented reasonably well with simple exponentials in  $\theta_{w,rms}^+$ , which are included in figure 7 and noted in its caption.

On comparing figures 5(a) and 5(b), we find that the transition from the low to the high Mach number limit in R1 for  $\gamma_{uv}$  is smoother than that of  $\gamma_{vv}$  for isothermal as well as

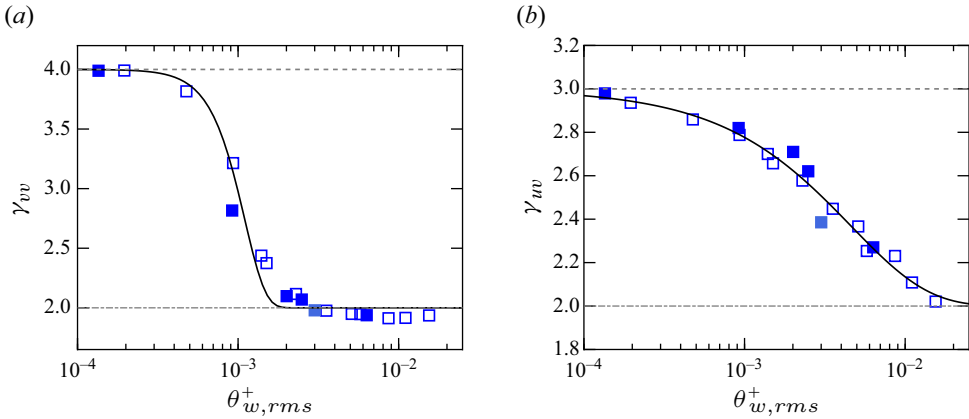


Figure 7. Power-law exponents in R1 for (a) wall-normal turbulent stress, (b) turbulent shear stress plotted against the r.m.s of dilatation at the wall. Markers as in table 3. Horizontal grey lines for solenoidal (dashed) and non-solenoidal (dash-dotted) asymptotic exponents (table 2). Solid lines are empirical correlations: (a)  $2 + 2 \exp(-10^{10} \theta_{w,rms}^{+3.38})$ , (b)  $2 + \exp(-126 \theta_{w,rms}^{+0.9})$ .

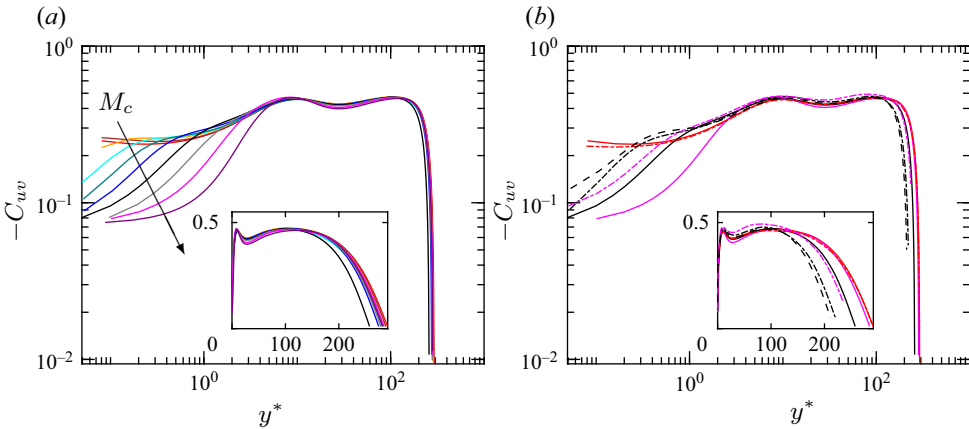


Figure 8. Correlation coefficient for  $R_{uv}$ : (a) isothermal wall; (b) isothermal (solid line), adiabatic (dash-dotted line) and pseudo-adiabatic (dashed line) walls. Inset contains the same data in linear scales. Colours as in table 1.

adiabatic cases (adiabatic cases exhibit an even slower transition than isothermal cases). A similar observation can also be made from figure 7, where the transition (with levels of dilatation at the wall in this case) is smoother for  $\gamma_{uv}$  as compared to  $\gamma_{vv}$ . This suggests a slow decorrelation between  $u'$  and  $v'$  as compressibility levels increase close to the wall. To study this, we show in figure 8(a) the correlation coefficient  $C_{uv} \equiv \overline{u'v'}/u_{rms}v_{rms}$  for all isothermal cases in the database. We similarly define the correlation coefficient  $C_{\alpha\beta}$  for arbitrary variables  $\alpha$  and  $\beta$  as

$$C_{\alpha\beta} \equiv \frac{\overline{\alpha'\beta'}}{\alpha_{rms}\beta_{rms}}. \tag{4.2}$$

We see that for the lowest Mach numbers,  $C_{uv}$  is relatively constant close to the wall ( $y^* \lesssim 1$ ). As  $M_c$  increases, the overall magnitude of the correlation is reduced in this region, though all the lines seem to approach a region of relatively constant correlation approximately 0.45, a value consistent with those observed in supersonic boundary layers (Shadloo *et al.* 2015). The distance from the wall at which this region starts, however, increases with  $M_c$ , indicating that compressibility effects are felt at increasing distance from the wall as the Mach number increases. The increasing decorrelation close to the wall with  $M_c$  has also been observed in Sciacovelli *et al.* (2017), an effect that was also found to be independent of Reynolds number. This near-wall decorrelation that becomes stronger as  $M_c$  increases suggests that while a simple product of Taylor expansions can describe diagonal stresses (e.g.  $R_{uu}$  or  $R_{vv}$ ), this is not the case for off-diagonal stresses ( $R_{uv}$ ), which comprise the correlation between two different variables. In particular, we see that for low and high  $M_c$ , the correlation  $C_{uv}$  is relatively constant close to the wall, though at different levels. It is at intermediate Mach numbers that  $C_{uv}$  presents a positive slope in this region. Thus because  $\overline{u'v'} = C_{uv}u_{rms}v_{rms}$ , we can see how the R1 exponent for  $R_{uv}$  would be close to the sum of the exponents for  $u_{rms}$  and  $v_{rms}$  for low and high  $M_c$ , while it would be larger at intermediate  $M_c$ . This explains, then, why the transition from the solenoidal to the non-solenoidal asymptotes is smoother for  $R_{uv}$  than for the case of diagonal stresses. At the centreline of the channel,  $C_{uv}$  vanishes due to reflective symmetry across the centreline plane, which is seen as a rapid decrease in the correlation in the figure at high values of  $y^*$ .

To assess the effect of WTBC, in figure 8(b) we show the correlation coefficient for different boundary conditions and three Mach numbers,  $M_c \approx 0.23, 1.2$  and  $1.9$ . As before, we see that  $C_{uv}$  is relatively flat at the lowest  $M_c \approx 0.23$  and for distances below  $y^* \sim \mathcal{O}(1)$ , with very little WTBC effect. The same weak dependence on WTBC is observed at  $y^*$  beyond, say, 4, where  $C_{uv}$  approaches the constant value discussed above. As the Mach number is increased, however, there are observable differences between isothermal, adiabatic and pseudo-adiabatic walls. In particular, we see that isothermal walls (black solid line) create a stronger decorrelation between  $u$  and  $v$  than adiabatic walls (black dash-dotted line) for  $M_c \gtrsim 1.2$  and pseudo-adiabatic (black dashed line) for  $M_c \approx 1.2$ . In addition, there are differences in the slope for  $C_{uv}$  close to the wall between adiabatic and isothermal cases, especially for  $M_c \approx 1.2$ , which also seem to contribute to the difference in power-law behaviour for these two WTBCs. This is clearly evident in figure 5(b), where  $\gamma_{vv}$  for  $M_c \approx 1.2$  seems to have the largest difference between isothermal and adiabatic cases. Moreover, the distance from the wall at which the constant region of  $C_{uv}$  starts is larger for isothermal than adiabatic cases.

Finally, in figure 9 we show the wall-normal location where  $R_{vv}$  and  $R_{uv}$  transition from region R1 to region R2, which is denoted as  $y_{lr}$ . This location is computed as the intersection of the corresponding power-law fits in R1 and R2. An example is shown in the inset of figure 9(a). Consistent with the results in Baranwal *et al.* (2022), we see in that  $y_{lr}$  moves away from the wall as  $M_c$  is increased. However, we also observe clear WTBC effects. In particular, we see that for adiabatic walls (dark-filled symbols), the transition moves closer to the wall compared to isothermal (empty symbols) and pseudo-adiabatic (light-filled symbols) walls. For example, for high  $M_c$ , we see close to order-of-magnitude differences in  $y_{lr}$  between isothermal and adiabatic cases for  $R_{vv}$ . As before (figures 7a,b), we can explore the suggestion in Donzis & Panickacheril (2020) that a higher degree of universal behaviour will be observed when dilatational motions are used to scale statistics of interest. This is indeed supported by the data in figure 9(b), where we show  $y_{lr}$  as a

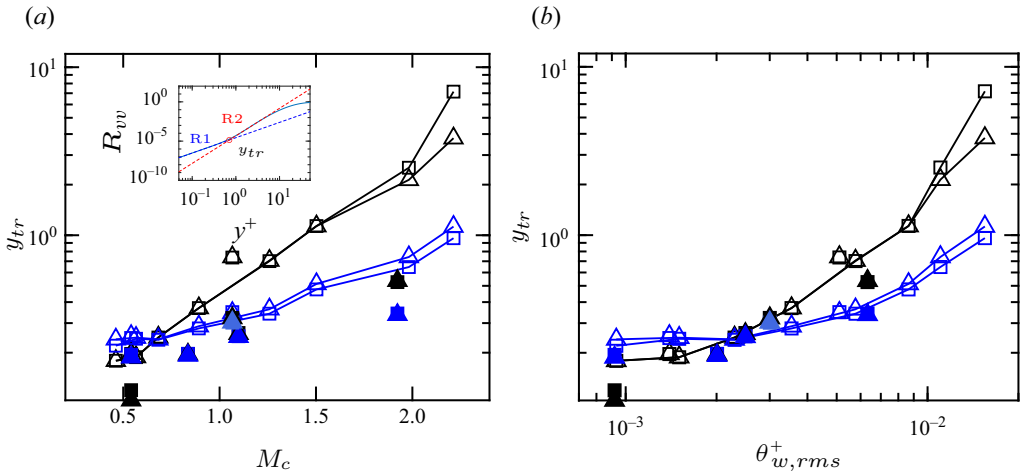


Figure 9. Transition location of scaling exponents plotted versus (a) centreline Mach number (inset shows power-law fits to  $R_{vv}$  in R1 and R2, and the transition location for  $M_c = 1.5$  near the isothermal wall), and (b) r.m.s dilatation at the wall. Markers: squares for  $y^+$ ; triangles for  $y^*$ ; black and blue correspond to wall-normal Reynolds stress and shear Reynolds stress, respectively, for isothermal (empty), adiabatic (dark-filled) and pseudo-adiabatic (light-filled) cases.

function of  $\theta_{w,rms}^+$ . Data for both  $R_{vv}$  and  $R_{uv}$  appear to be closer to exhibiting universal scaling (though not perfect) under this normalization.

We can then conclude that by increasing the centreline Mach number, or changing any other flow condition that results in enhancing dilatation levels at the wall, an enlarged region close to the wall will develop where compressibility effects are significant. This is also the region where Morkovin’s hypothesis is found to be inadequate to collapse Reynolds stresses, as shown before.

### 5. Effects of thermal boundary conditions on temperature fluxes

The asymptotic behaviour of temperature can be analysed in a similar way to the velocity field by considering separately isothermal and adiabatic conditions. The Taylor series expansion of temperature fluctuations is given by

$$T' = a_T + b_T y + c_T y^2 + \dots \tag{5.1}$$

For the isothermal case, temperature is fixed at the wall, and one has  $a_T = 0$  (but  $b_T \neq 0$ ). For the adiabatic case, there are fluctuations at the wall, but its normal gradient vanishes, in which case  $b_T = 0$  (but  $a_T \neq 0$ ). One would thus expect different near-wall asymptotic behaviour based on thermal boundary conditions. In figure 10(a), we plot the r.m.s. of temperature  $T_{rms}$  normalized by the mean wall temperature  $T_w$  against  $y^*$  for all cases. We find that the asymptotic behaviour of  $T_{rms}$  is qualitatively different for isothermal and adiabatic walls. Near the isothermal wall,  $T_{rms}$  follows a power-law increase, while the adiabatic cases are flat. Similar asymptotic behaviour was observed in incompressible and low-Mach-number flows for isothermal and isoflux conditions (Tiselj *et al.* 2001; Li *et al.* 2009). The asymptotic power-law scaling for isothermal cases is equal to its theoretical asymptote ( $\gamma_T = 1$ ) for all  $M_c$ . For adiabatic cases, the profile is constant for most of the viscous sublayer (until  $y^* \approx 2$ ), and that constant increases with increase in  $M_c$ . Interestingly, the pseudo-adiabatic case (black dashed line), which has been extensively used in the literature

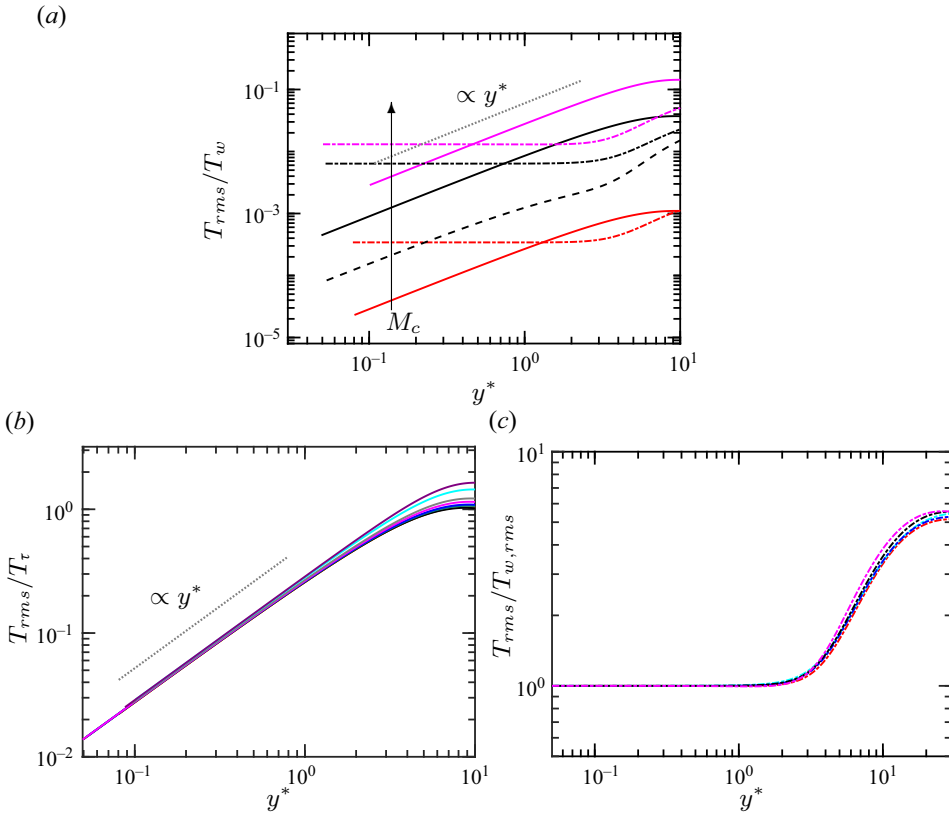


Figure 10. The r.m.s. temperature fluctuations: (a) normalized with wall temperature for isothermal (solid line), adiabatic (dash-dotted line) and pseudo-adiabatic (dashed line) cases; (b) normalized with friction temperature for isothermal cases; (c) normalized with r.m.s. temperature at the adiabatic wall for adiabatic cases. Red, black and magenta correspond to  $M_c \approx 0.23$ ,  $M_c \approx 1.2$  and  $M_c \approx 1.9$ , respectively.

to model adiabatic walls, exhibits an isothermal-like power-law behaviour close to the wall.

An alternative normalization for temperature, in analogy with the Reynolds stresses, is through the so-called friction temperature,  $T_\tau \equiv -\kappa(\partial\bar{T}/\partial y)_w/\bar{\rho}_w c_p u_\tau$ , where  $\kappa$  is the thermal conductivity. It is clear, however, that this normalization can be applied only to isothermal walls, since adiabatic (and pseudo-adiabatic) walls present zero conductive heat transfer to the wall ( $\partial\bar{T}/\partial y|_w = 0$ ). In figure 10(b), we show all isothermal cases that do, in fact, collapse in the near-wall region following its asymptotic scaling of  $\sim y^*$ . A collapse of adiabatic cases is also obtained when  $T_{rms}$  is normalized with their respective wall values ( $T_{w,rms}$ ) as seen in figure 10(c). Since  $T_{w,rms} = 0$  for isothermal cases, it is clear that neither normalization provides universal scaling across different WTBCs.

### 5.1. Streamwise turbulent heat flux

The streamwise component of the turbulent heat flux ( $R_{uT}$ ) is an important quantity in wall-bounded flows, which needs to be correctly modelled in order to make accurate predictions. In fact, this heat flux component has been found to be even larger than the wall-normal turbulent heat flux (Huang *et al.* 2020). Current Boussinesq or constant  $Pr_T$

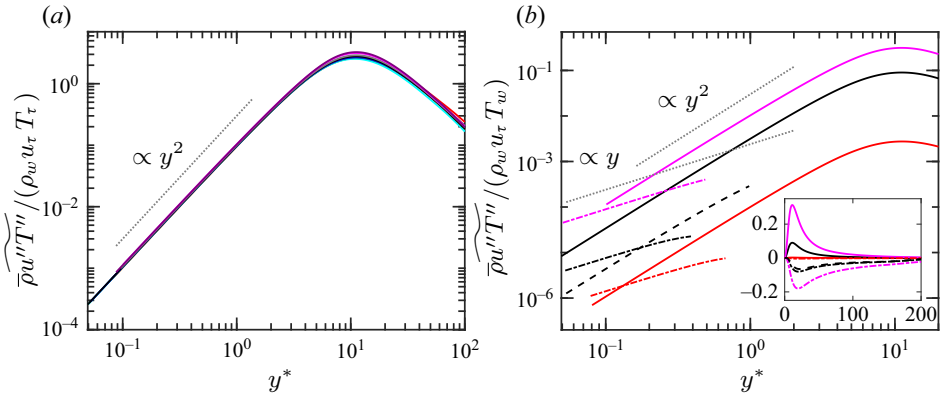


Figure 11. Streamwise turbulent heat flux close to: (a) isothermal walls normalized by friction temperature; (b) isothermal (solid line), adiabatic (dash-dotted line) and pseudo-adiabatic (dashed line) cases normalized by their respective wall temperature. The inset contains the same data in linear scales up to  $y^* \approx 200$ . Red, black and magenta correspond to  $M_c \approx 0.23$ ,  $M_c \approx 1.2$  and  $M_c \approx 1.9$ , respectively.

based RANS models, however, cannot capture its behaviour accurately (Bowersox 2009; Huang *et al.* 2019; Broslawski *et al.* 2022).

In figure 11(a), we show the density-scaled streamwise turbulent heat flux,  $\overline{\rho u'' T''} / (\rho_w u_\tau T_\tau)$  in the near-wall region of an isothermal wall for different Mach numbers against  $y^*$ . We observe very good collapse for all Mach numbers along the theoretical asymptotic power law given by  $\gamma_{uT} = 2$  (table 2). The adiabatic and pseudo-adiabatic cases are included in figure 11(b) (normalized with mean wall temperature) along with the isothermal cases for comparison. The temperature fluctuations at the wall for adiabatic cases result in  $\gamma_{uT} = 1$  and again conform to the theoretical behaviour. Following  $T_{rms}$ , we observe that power-law behaviour for pseudo-adiabatic streamwise heat flux follows isothermal-like behaviour and thus also matches with the isothermal theoretical exponent. The streamwise heat flux becomes negative for  $y^* \gtrsim 1$  in adiabatic and pseudo-adiabatic cases, and thus can not be shown in logarithmic scales. Again, this indicates that fine resolution close to the wall is required to capture correct near-wall asymptotic behaviour. In the inset of figure 11(b), we also include the streamwise heat flux across the channel in linear scales. Similar to  $T_{rms}$ , we find that normalization by neither  $T_w$  nor  $\bar{T}$  (not shown here) leads to a collapse of  $R_{uT}$  for different  $M_c$  and WTBCs in the high-speed regime.

Similar to the case of  $R_{uv}$  discussed above, the near-wall asymptotic behaviour of  $R_{uT}$  will depend not only on the scaling of the r.m.s. of the two variables involved in the flux, but also on their cross-correlation. The excellent agreement seen for  $\gamma_{uT}$  for all cases with their respective theoretical scaling, then, implies that the correlation coefficient  $C_{uT}$  does not vary in  $y$  in this region, and is evident in figure 12. For  $y^* \lesssim 1$ ,  $C_{uT}$  is constant with  $y^*$  for all  $M_c$  and WTBCs. However, we see interesting differences between different WTBCs. First, the absolute value of  $C_{uT}$  is minimum near the wall for adiabatic cases, while for isothermal cases, the absolute value of  $C_{uT}$  is maximum close to the wall. Some  $M_c$  effects can be observed for adiabatic cases close to the wall, while  $-C_{uT}$  for different  $M_c$  collapses to a constant value  $-1$  near isothermal walls. For adiabatic cases, the decorrelation decreases on moving away from the wall until  $y^* \approx 15$ , while  $C_{uT}$  for isothermal cases remains constant in this region, with  $-C_{uT} \approx -1$ . Interestingly, the

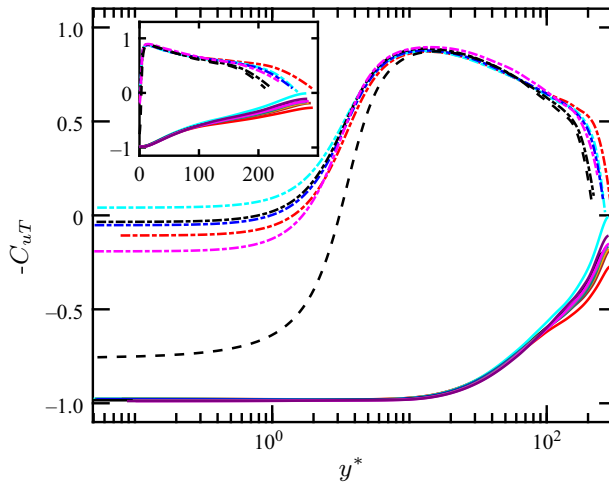


Figure 12. Correlation coefficient for  $R_{uT}$  for isothermal (solid line), adiabatic (dash-dotted line) and pseudo-adiabatic (dashed line) cases. Colours as in table 1. The inset contains the same data in linear scales.

pseudo-adiabatic case resembles isothermal-like behaviour near the wall and adiabatic-like behaviour beyond  $y^* \approx 10$ . At further distance,  $y^* \gtrsim 15$ , decorrelation increases for all WTBCs, with the isothermal case maintaining a positive correlation, while adiabatic and pseudo-adiabatic cases maintain negative correlations ( $C_{uT}$ ). The correlation's magnitude decreases as one moves towards the centreline. Another interesting observation from figure 12 is that  $C_{uT}$  for adiabatic and pseudo-adiabatic cases, as shown in the inset of figure 12, resembles the  $C_{uT}$  profile for a flat-plate boundary layer (Duan *et al.* 2010) with isothermal or pseudo-adiabatic walls.

### 5.2. Wall-normal turbulent heat flux

In figure 13(a), we plot the density-averaged wall-normal turbulent heat flux ( $R_{vT}$ ),  $\overline{\rho v'' T''} / (\rho_w u_\tau T_w)$  close to the wall for isothermal cases (solid lines) with  $M_c \approx 0.23, 1.2, 1.9$ , low Mach adiabatic case with  $M_c \approx 0.23$ , and pseudo-adiabatic case with  $M_c \approx 1.2$ . It can be seen that close to the isothermal wall, a Mach-number-dependent power law exists for the wall-normal turbulent heat flux. A detailed study of the asymptotic power law for wall-normal turbulent heat flux close to isothermal walls was performed in Baranwal *et al.* (2022), where power-law exponents were observed to transition from its theoretical low Mach to high Mach asymptotes. This transition was found to be similar to that of  $\gamma_{uv}$ . The asymptotic behaviour of heat flux close to the pseudo-adiabatic wall exhibits a power-law behaviour with  $\gamma_{vT} \approx 2.1$ , and matches closely to the theoretical limit of the isothermal asymptotic power law. This is in line with the behaviour of all other statistics close to the pseudo-adiabatic wall that behave like those in isothermal cases. For Mach number in the near-incompressible range  $M_c = 0.23$ , a power-law behaviour with exponent equal to its theoretical value is observed close to the adiabatic wall. Similar to  $R_{uT}$ ,  $R_{vT}$  changes sign as we move away from the wall for these adiabatic ( $M_c = 0.23$ ) and pseudo-adiabatic cases, and therefore cannot be shown in logarithmic scales. For adiabatic cases with  $M_c > 0.23$ , we find that  $R_{vT}$  remains very close to zero and then becomes negative (that is why it is shown in linear scales in figure 13b) at a location and to a level that depend on  $M_c$ . To explain the near-wall behaviour, consider the derivative  $\partial(\overline{v'T'})/\partial y|_w$  at the wall, which can be expanded to  $\overline{T'(\partial v'/\partial y)}|_w + \overline{v'(\partial T'/\partial y)}|_w$ . For

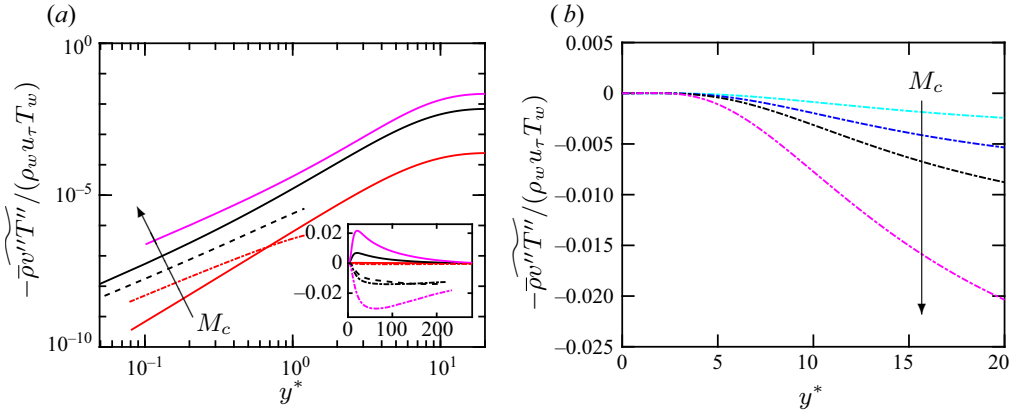


Figure 13. (a) Wall-normal turbulent heat flux close to isothermal (solid line), adiabatic (dash-dotted line) and pseudo-adiabatic (dashed line) walls in logarithmic scale. Inset contains the same data in linear scales up to  $y^* \approx 300$ . Red, black and magenta correspond to  $M_c \approx 0.23$ ,  $M_c \approx 1.2$  and  $M_c \approx 1.9$ , respectively. (b) Wall-normal turbulent heat flux close to adiabatic walls in linear scales. Colours as in table 1.

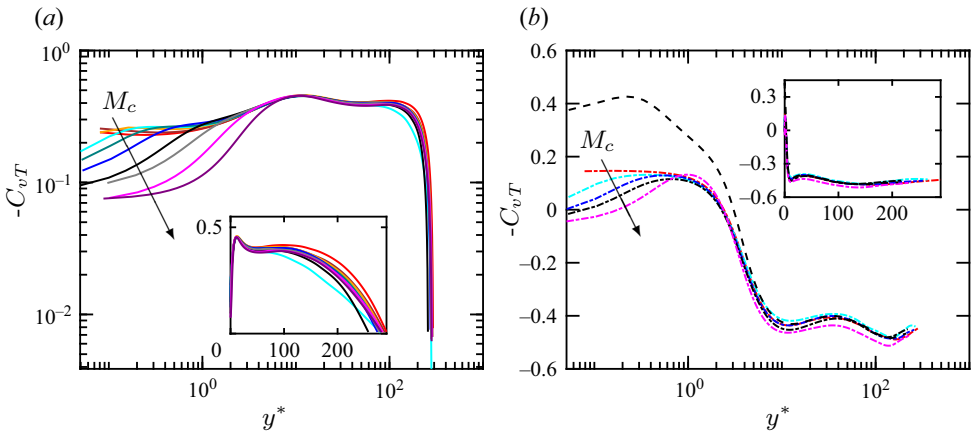


Figure 14. Correlation coefficient for  $R_{vT}$  near (a) isothermal walls, (b) adiabatic (dash-dotted line) and pseudo-adiabatic (dashed line) walls. The inset contains the same data in linear scales. Colors as in table 1.

adiabatic cases,  $\partial T'/\partial y|_w$  vanishes, and therefore so does the second term in the previous equation. Furthermore, since  $\partial v'/\partial y|_w = \theta_w$ , we have  $\partial(\overline{v'T'})/\partial y|_w \approx \overline{T'\theta'}|_w$ . We now see that when temperature fluctuations are uncorrelated with dilation fluctuations at the wall, we would expect a flat region such as that seen in figure 13(b) only for adiabatic cases. We will momentarily see that indeed this correlation plays a key role in the heat flux close to the wall. Similar to  $T_{rms}$  and  $R_{uT}$ , we find that normalization using neither  $T_w$  nor  $\overline{T}$  (not shown here), succeeds in collapsing  $R_{vT}$  for different  $M_c$  and WTBC in high-speed regimes.

Finally, we plot  $-C_{vT}$  as a function of  $y^*$  in figure 14. For isothermal cases as shown in figure 14(a),  $C_{vT}$  closely resembles  $C_{uv}$  as shown in figure 8, indicating that increasing  $M_c$  has similar effects on  $C_{vT}$  as were observed for  $C_{uv}$ . In the inset of figure 14(a), we plot  $C_{vT}$  in linear scales, where moving towards the centreline ( $y^* \gtrsim 100$ ), some Mach

number effects can be observed. For adiabatic walls, as shown in figure 14(b), a trend with the Mach number close to the wall is observed for  $C_{vT}$ . On moving away from the wall, the decorrelation between  $v'$  and  $T'$  decreases. Furthermore, the effect of mixed boundary condition can be observed close to the channel centreline, where  $C_{vT}$  does not vanish. This is because of the finite mean temperature gradients at the channel half-width resulting in the non-zero wall-normal heat flux at  $h$ . On comparing figures 14(a) and 14(b), we observe that  $C_{vT}$  assumes opposite signs for isothermal and adiabatic cases in regions away from the wall. Like the previous observation for other statistics close to the wall, pseudo-adiabatic exhibits isothermal-like near-wall behaviour but follows adiabatic in regions away from the wall.

We now come back to the flat behaviour of  $R_{vT}$  close to the wall (figure 13b). As suggested above and consistent with with figure 14, we see that as Mach number increases, the correlation between temperature and dilatation decreases as the latter becomes stronger by e.g. increasing  $M_c$ . This will also be clearly seen in the next section where the patterns of  $\theta'$  are closely followed by  $v'$ , while temperature resembles more the streamwise velocity. Thus it appears that the dynamics of temperature fluctuations, even very close to the wall, may follow Navier–Stokes dynamics, while dilatation at the wall (and thus  $v'$ ) is strongly affected by kinematics of boundary conditions.

## 6. Flow structure

In order to get a better understanding of the flow characteristics in the near-wall region, and in particular the relation between variables, we show contours of the key variables (velocity and temperature fluctuations, Reynolds stress, heat fluxes and dilatation) at two distances from the wall, namely,  $y^+ \approx 0.15$  and  $y^+ \approx 4$  (which are approximately representative of R1 and R2, respectively), at two Mach numbers, and for different WTBCs.

Figures 15 and 16 show data at  $M_c = 0.2$ , the lowest Mach number in the database (almost incompressible), at  $y^+ \approx 0.15$  and  $y^+ \approx 4$ , respectively. We can see that structures at these two locations are similar. This may not be surprising given that, as we showed in § 4, R1 and R2 fuse into a single scaling range in the incompressible limit. In general, we see that  $u'$ ,  $v'$  and  $T'$  exhibit streak-like structures in the streamwise direction, consistent with observation made in the literature (Shadloo *et al.* 2015; Chen & Scalò 2021; Cogo *et al.* 2022). We observe that while  $u'$  and  $T'$  exhibit longer streaks,  $v'$  has shorter and thinner structures that result in strong fluctuations forming clusters surrounded by large relatively quiet regions. While the structures look similar at the two distances from the wall, we find that fluctuations at  $y^+ \approx 4$  are much stronger, as expected.

Interestingly, for  $M_c \approx 0.2$ ,  $u'$  and  $T'$  are strongly correlated to each other (seen by the correspondence of high/low-speed velocity with high/low temperature zones) for the isothermal cases at both wall-normal locations. For adiabatic cases, streaks become wider in the spanwise direction and look less coherent for temperature fluctuations. In addition,  $u'$  and  $T'$  appear less correlated in adiabatic than isothermal cases. This is in accordance to our results for  $C_{uT}$  in figure 12, where we see that close to the wall, the correlation is close to unity for isothermal walls, while it takes a much smaller value for adiabatic walls. For fluxes containing the wall-normal component of velocity, namely,  $u'v'$  and  $v'T'$ , structures resemble more  $v'$  than  $u'$  or  $T'$  for both isothermal and adiabatic. Discerning the correlations between  $v'$  and  $u'$ , and  $v'$  and  $T'$ , from these kind of visualizations is naturally difficult. The quantitative counterpart, which provides a consistent view of these observations, was shown above in the form of correlation coefficients. The signature of dilatation, characterized by structures elongated in the spanwise direction, are not present in any of the other fluctuating variables at low  $M_c$ .

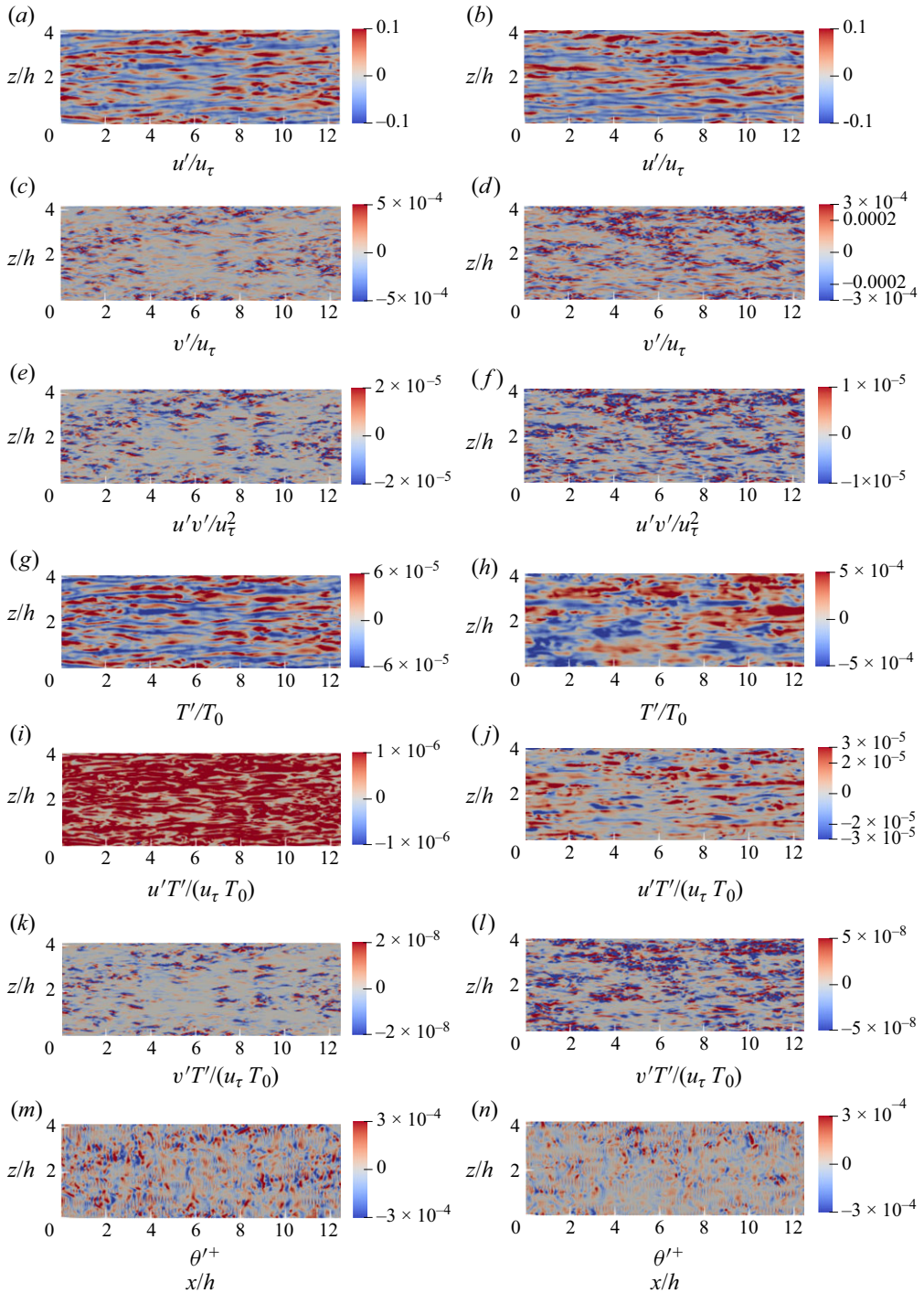


Figure 15. Normalized instantaneous (a,b) streamwise velocity fluctuations, (c,d) wall-normal velocity fluctuations, (e,f) Reynolds shear stress, (g,h) temperature fluctuations, (i,j) streamwise turbulent heat flux, (k,l) wall-normal turbulent heat flux, (m,n) dilatation fluctuations, shown in the  $x-z$  plane at  $y^+ \approx 0.15$  near (a,c,e,g,i,k,m) isothermal and (b,d,f,h,j,l,n) adiabatic walls for  $M_c \approx 0.2$ .

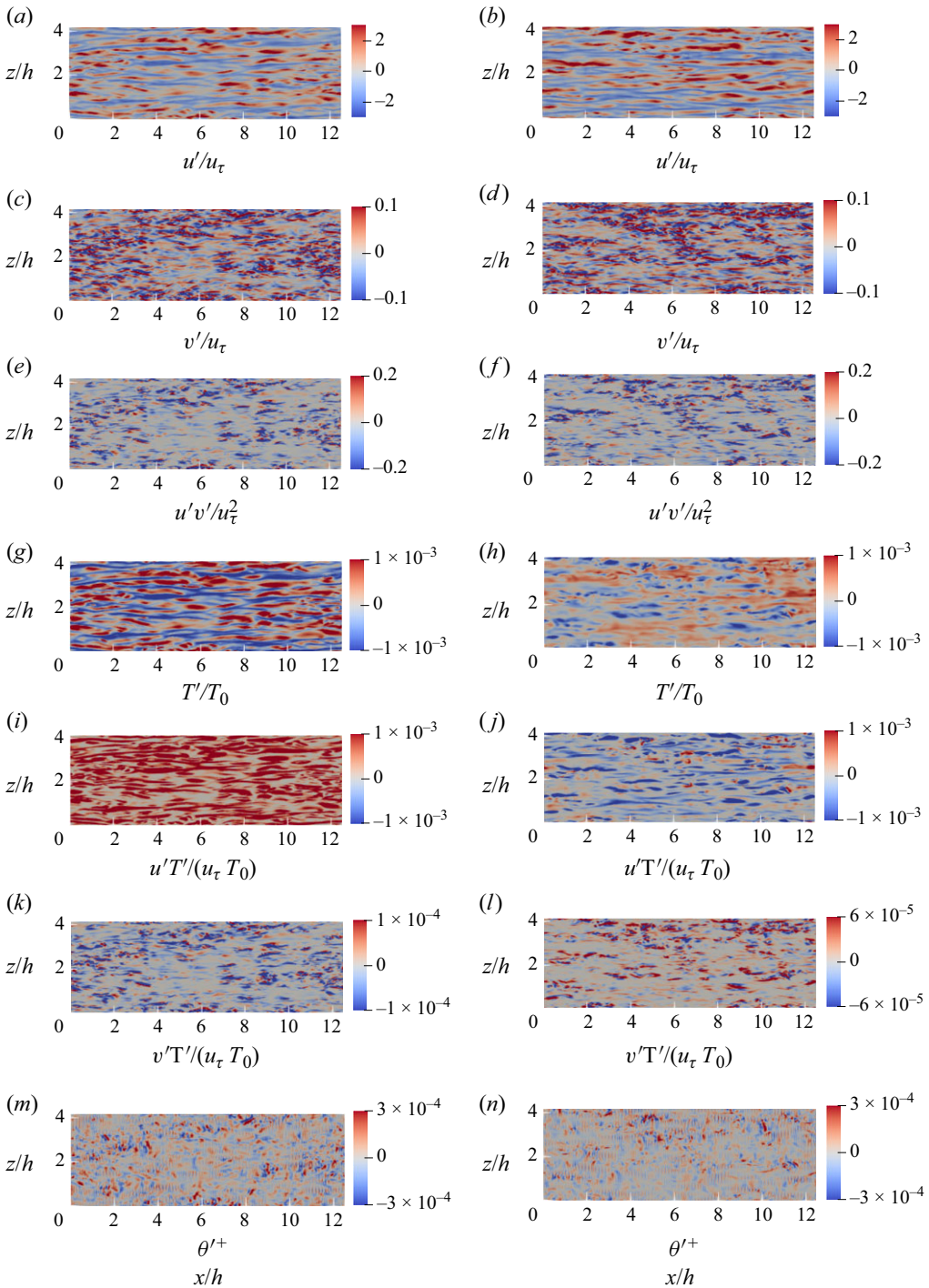


Figure 16. Normalized instantaneous (a,b) streamwise velocity fluctuations, (c,d) wall-normal velocity fluctuations, (e,f) Reynolds shear stress, (g,h) temperature fluctuations, (i,j) streamwise turbulent heat flux, (k,l) wall-normal turbulent heat flux, (m,n) dilatation fluctuations, shown in the  $x-z$  plane at  $y^+ \approx 4$  near (a,c,e,g,i,k,m) isothermal and (b,d,f,h,j,l,n) adiabatic walls for  $M_c \approx 0.2$ .

On increasing Mach number (figure 17), we see that for the isothermal case at  $y^+ \approx 0.15$ ,  $u'$  and  $T'$  still maintain streak-like structures, though  $v'$  acquired signatures of dilatation with spanwise-aligned structures. Similar to observations in hypersonic boundary layers (Xu *et al.* 2021a,b; Yu *et al.* 2024), we also see that  $\theta'$  exhibits small structures forming sign-alternating patterns along the streamwise direction. Several studies (Yu *et al.* 2019; Xu *et al.* 2021a) used the Helmholtz decomposition to split the wall-normal velocity into solenoidal and dilatational parts to show that close to the wall, the latter are higher than the former. Both the total as well as the dilatational component of the wall-normal velocity exhibit spanwise ripples that resemble the structures observed for  $\theta'$ . Here, we can see that these effects are evident in channel flows even at fairly low supersonic speed  $M_c \approx 1.2$ . These signatures of  $\theta'$  acquired by  $v'$  can also be observed in fluxes containing the normal velocity, namely,  $u'v'$  and  $v'T'$ . The implication of these observations is that very close to the wall, dilatation can change the structure of fluxes containing the wall-normal component of velocity. We also find very small weak structures of the size of the grid for fluxes containing  $v'$ . Our grid convergence studies (Appendix A), however, show that they do not affect the scaling of Reynolds stresses and their slopes.

On changing the thermal condition at the wall, we can see differences between the streaks formed in isothermal, adiabatic and pseudo-adiabatic cases (figure 19) for  $u'$  and  $T'$ . In particular, changing from isothermal to adiabatic or pseudo-adiabatic, the streaks become wider in the spanwise direction and look less coherent for temperature fluctuations, as was observed for  $M_c \approx 0.2$  in figure 15. The effect of changing WTBC from isothermal to adiabatic seems more dramatic for  $M_c \approx 1.2$  than for  $M_c \approx 0.2$ . This effect also emerges in streamwise velocity fluctuations, where streaks become wider in the spanwise direction due to the increased coupling between thermodynamics and hydrodynamics at higher Mach numbers. The effect of changing WTBC on the coherence of near-wall streak was also reported by Xu *et al.* (2021a) where, consistent with our results, they showed an increase in coherency with cold walls.

Similar to the isothermal case, wave-like alternating positive and negative structures of  $\theta'$  and their influence on  $v'$ ,  $u'v'$  and  $v'T'$  can also be observed for adiabatic and pseudo-adiabatic conditions. However, the spacing between the structures with positive and negative values is increased (or alternatively the frequency of these wave-like structures is decreased) for the adiabatic and pseudo-adiabatic relative to the isothermal case.

Comparing figures 17 and 18 shows that going from R1 to R2 ( $y^+ \approx 0.4$ ) does not lead to changes in  $u'$  as one moves away from the wall for all WTBCs, consistent with what was observed for  $M_c \approx 0.2$ . However, the normal velocity  $v'$  organizes itself into streak-like shorter and thinner structures in the streamwise direction for all WTBCs as was seen for  $v'$  in figure 16, thus losing the structural patterns observed for  $\theta'$ . Because  $u'v'$  and  $v'T'$  also resemble the patterns of  $v'$ , they also lose the signature patterns of dilatation. Correspondingly, they appear similar to their corresponding structures in the low Mach number case in figure 16. This also follows our observation that there is better collapse of  $R_{vv}$  and  $R_{uv}$  in R2 than in R1 (figure 4) as one changes both Mach number and WTBC. We also note that with an increase in dilatation levels, as shown in figure 9(b), the transition from R1 to R2 moves further from the wall. In this case,  $v'$  acquires signatures of dilatational structures that penetrate deeper into the flow. This can also be seen in the results from Xu *et al.* (2021a) at high Mach numbers ( $M = 8$ ), where  $v'$  resembles dilatation at distances as far as  $y^+ \approx 10$ .

In summary, these visualizations provide a strong corroboration of our results, suggesting that fluxes containing the wall-normal velocity show deviations from their incompressible counterpart, with dilatation providing the key to characterize this seemingly universal behaviour.

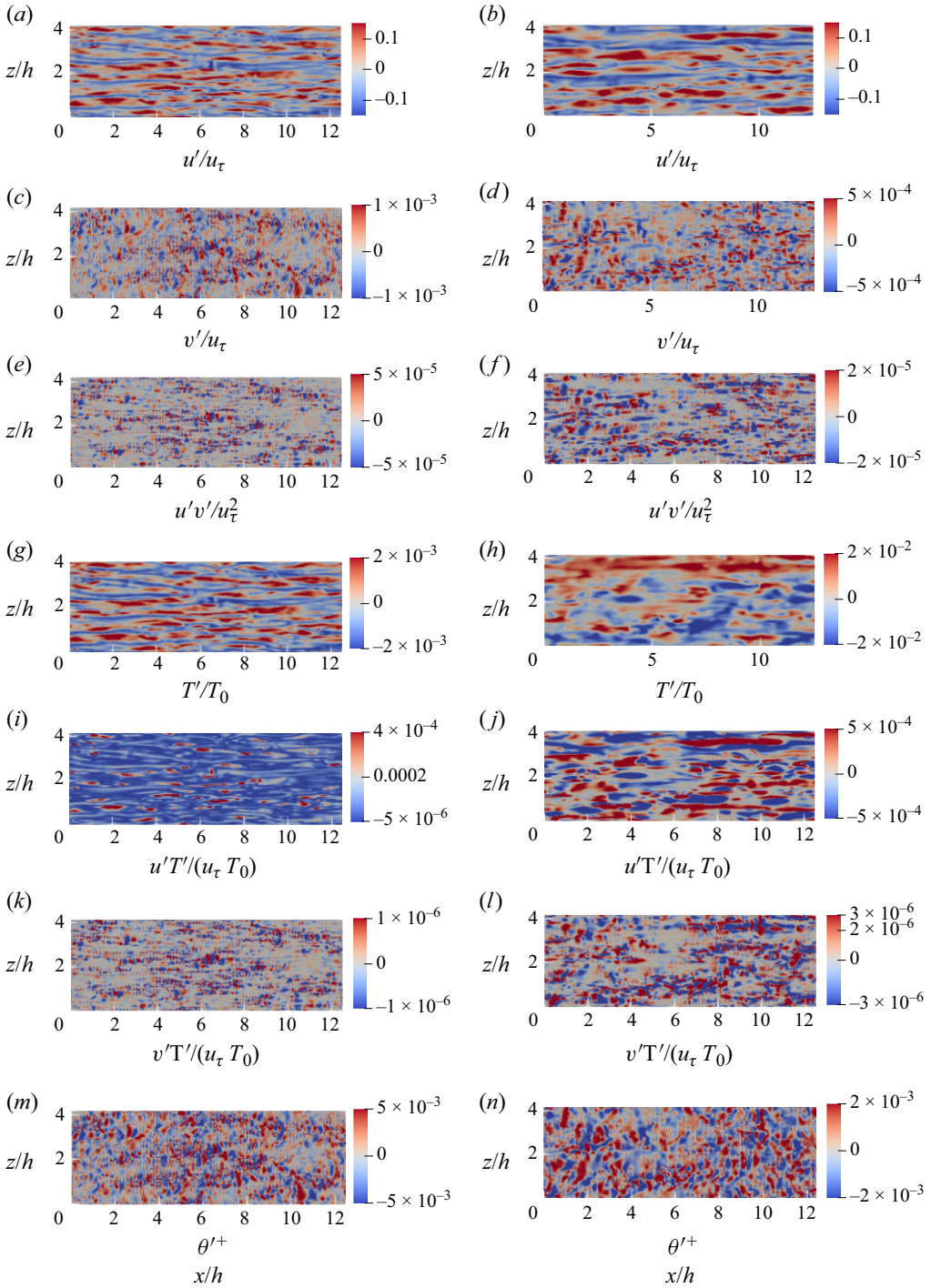


Figure 17. Normalized instantaneous (a–b) streamwise velocity fluctuations, (c–d) wall-normal velocity fluctuations, (e–f) Reynolds shear stress, (g–h) temperature fluctuations, (i–j) streamwise turbulent heat flux, (k–l) wall-normal turbulent heat flux, (m–n) dilatation fluctuations, shown in the  $x-z$  plane at  $y^+ \approx 0.15$  near (a, c, e, g, i, k, m) isothermal, (b, d, f, h, j, l, n) adiabatic walls for  $M_c \approx 1.2$ .

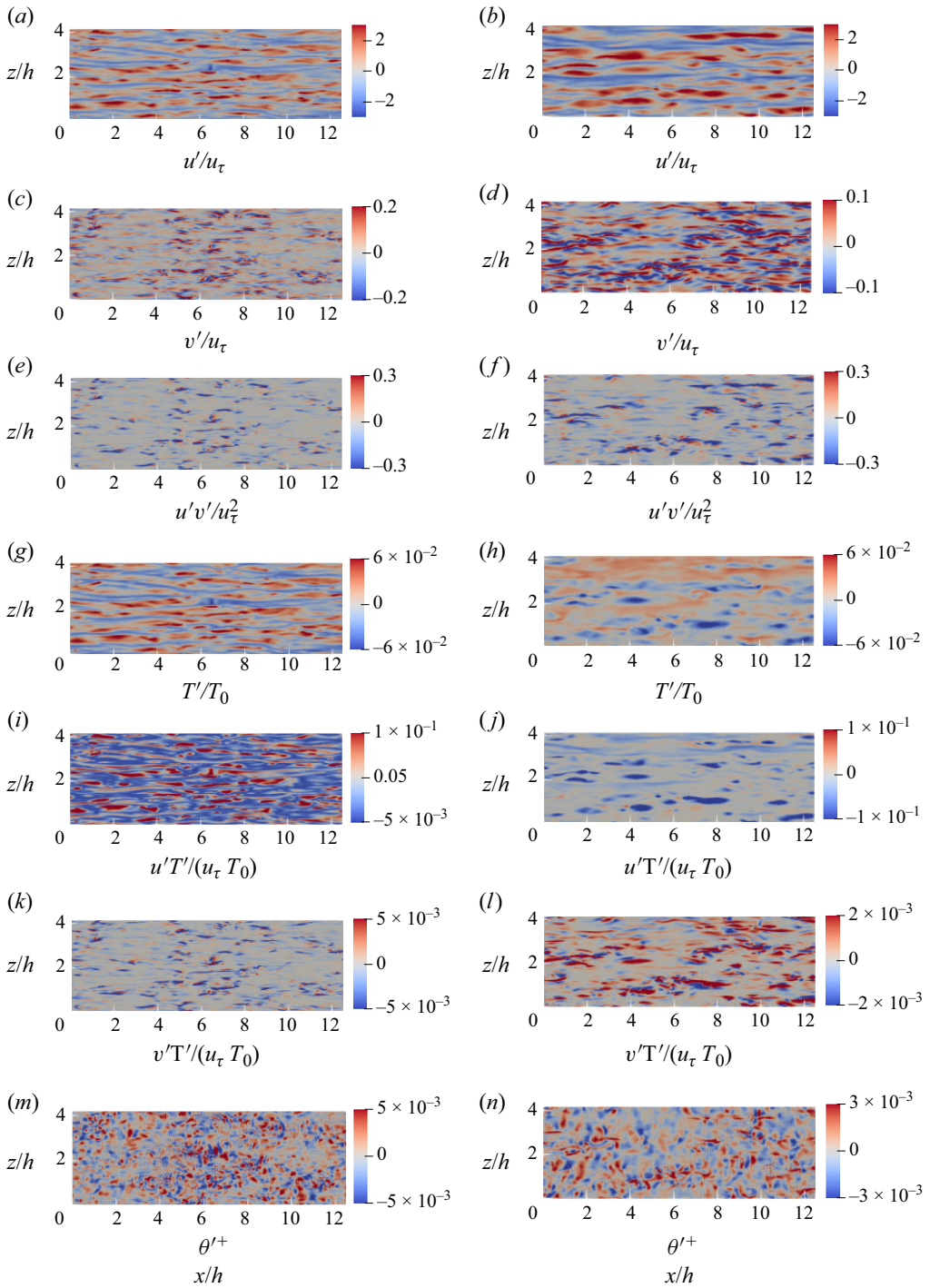


Figure 18. Normalized instantaneous (a–b) streamwise velocity fluctuations, (c–d) wall-normal velocity fluctuations, (e–f) Reynolds shear stress, (g–h) temperature fluctuations, (i–j) streamwise turbulent heat flux, (k–l) wall-normal turbulent heat flux, (m–n) dilatation fluctuations, shown in the  $x-z$  plane at  $y^+ \approx 0.4$  near (a,c,e,g,i,k,m) isothermal, (b,d,f,h,j,l,n) adiabatic walls for  $M_c \approx 1.2$ .

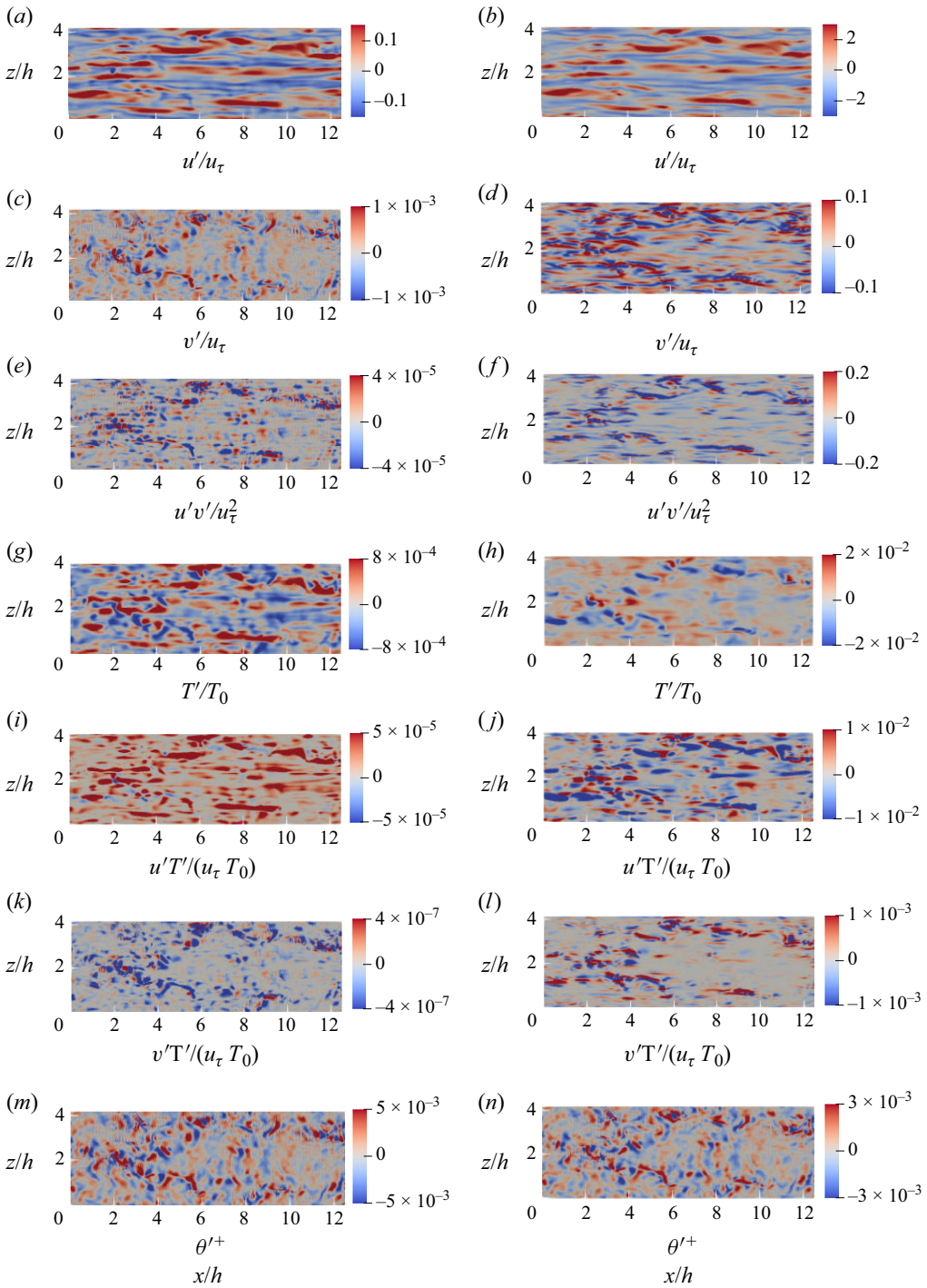


Figure 19. Normalized instantaneous (a,b) streamwise velocity fluctuations (c,d) wall-normal velocity fluctuations (e,f) Reynolds shear stress (g,h) temperature fluctuations (i,j) streamwise turbulent heat flux (k,l) wall-normal turbulent heat flux (m,n) dilatation fluctuations shown in the  $x - z$  plane at (a,c,e,g,i,k,m)  $y^+ \approx 0.15$  and at (b,d,f,h,j,l,n)  $y^+ \approx 4$  near pseudo-adiabatic walls for  $Mc \approx 1.2$ .

## 7. Conclusions and outlook

The asymptotic behaviour of turbulent stresses and turbulent heat fluxes close to the wall was investigated using a large DNS database of turbulent channel flows with centreline Mach numbers spanning from 0.23 to 2.22. The dataset comprises simulations with three different wall thermal boundary conditions (WTBCs), namely isothermal, adiabatic and pseudo-adiabatic. A distinguishing feature of the present DNS is the near-wall resolution, which is much finer than those typically found in the literature. We show that this is essential to capture near-wall behaviour for different flow and wall boundary conditions.

Turbulent stresses containing a wall-normal velocity component do not exhibit a universal behaviour close to the wall when normalized using either wall or semi-local units. Interestingly, some statistics behave differently for different WTBCs, while others behave similarly. Similarities include Mach number effects on statistics close to the wall for isothermal and adiabatic cases. In both cases, turbulent stresses exhibited asymptotic power-law behaviour in the near-wall region (which we call R1) for all Mach numbers and WTBCs. With increase in Mach number, smooth transition of asymptotic power-law exponents from the solenoidal limit to the high-speed limit was observed. Consistent with previous findings, a second scaling regime (R2) with a steeper exponent and a weaker Mach number dependence beyond R1 was observed. The transition location between R1 and R2 was dependent on Mach number.

A notable difference between cases with different WTBCs is the change in power-law exponents for turbulent stresses with changing WTBC at high Mach numbers. This effect is stronger for  $R_{uv}$  than for  $R_{vv}$ . In general,  $R_{uv}$  was found to be more sensitive to changes in  $M_c$  or WTBC. This was linked to a decorrelation between  $u'$  and  $v'$  when  $M_c$  is increased or when the WTBC changes from isothermal to adiabatic.

Inspired by a recent proposal based on homogeneous flows, we found that universality can indeed be recovered if dilatational motions are incorporated as a governing parameter, regardless of the mechanism that generated them. In particular, asymptotic power-law exponents and the transition location between the two scaling regimes R1 and R2 do collapse on a universal curve that depends uniquely on  $\theta_{w,rms}$ , the r.m.s. of dilatation at the wall. If one uses the (perhaps more intuitive) centreline Mach number, then one can clearly see differences in exponents and transition location for different WTBCs. This clearly supports the idea that dilatational levels, regardless of how they are generated, provide the appropriate scaling parameter for near-wall behaviour at high speeds, furthering the idea of some universality of statistics in compressible wall-bounded flows. This also supports the previously found conclusion that Morkovin's hypothesis does not take into consideration all the effects associated with compressibility at higher Mach numbers.

We also investigated statistics of temperature fluctuations, wall-normal and streamwise turbulent heat fluxes for varying  $M_c$  and WTBC. For isothermal cases, we found that  $T_{rms}$  follows a power-law behaviour predicted by the analytical form of its Taylor expansion. For adiabatic cases, on the other hand,  $T_{rms}$  remains constant in the viscous sublayer followed by an almost universal increase with  $y^*$ .

The streamwise heat flux  $R_{uT}$  exhibits a power-law behaviour close to the wall, with exponents given by theoretical predictions for both isothermal and adiabatic cases. In general, it was found that temperature statistics ( $T_{rms}$ ,  $R_{uT}$ ) can be collapsed separately for isothermal and adiabatic cases by normalizing temperature with  $T_\tau$  and  $T_{w,rms}$ , respectively. However, no general scaling laws were found that could collapse statistics containing temperature fluctuations for both WTBCs.

As with Reynolds stresses, the wall-normal turbulent heat flux ( $R_{vT}$ ) for isothermal cases exhibits power-law behaviour with exponents that depend on  $M_c$ . A well-defined

power-law behaviour cannot be identified unambiguously for adiabatic cases with  $M_c > 0.23$ . Pseudo-adiabatic walls, which are often used to mimic an adiabatic wall by imposing an isothermal condition at the adiabatic temperature, displayed isothermal-like behaviour close to the wall as  $M_c$  increases. A rich interplay between Mach number and WTBC effects was observed for correlation coefficients between  $v'$  and  $T'$ , and between  $u'$  and  $T'$ , indicating a complex dynamics between velocity and temperature fluctuations.

Mach number effects were observed in the viscous sublayer for the correlation between  $v'$  and  $T'$  for all WTBCs, but only in the adiabatic case for  $u'$  and  $T'$ . The strong WTBC effect is evident by the fact that these correlations possess different signs in most of the region across the channel. In these regions,  $v'$  and  $T'$  are negatively correlated for isothermal walls, while they are positively correlated for adiabatic cases. In contrast,  $u'$  and  $T'$  are positively correlated for isothermal walls, but negatively correlated for adiabatic cases. Moreover, in the region close to the wall, the magnitudes of these  $u'$  and  $T'$  correlations are very different for isothermal and adiabatic cases, with the former being much stronger than the latter. Similar to all other statistics, the pseudo-adiabatic case exhibits isothermal-like near-wall behaviour but resembles the adiabatic profile away from the wall.

We close by pointing out that, overall, Morkovin's hypothesis and semi-local normalizations do not collapse data for all the flow and boundary conditions. Universal scaling laws for wall-bounded compressible flows thus require more general scaling laws. Universal scaling laws of this nature can have a direct impact on the formulation of physics-based models. First, one can require that the model should properly satisfy asymptotic behaviour at the wall. The strategy of anchoring models to the exact asymptotic behaviour at the wall has been used extensively in incompressible turbulence to evaluate e.g. RANS models. In compressible turbulence, this has not been addressed in a systematic way (hence the impetus for this work). This is particularly critical when different WTBCs are considered, as in the case of supersonic and hypersonic conditions (also part of this work). The second element from this work that is relevant to modelling is the evidence of a universal description of exponents across Mach numbers and WTBCs when levels of dilatation at the wall are used as the relevant parameter to characterize these exponents. Our finding of a universal transition from solenoidal to compressible exponents that can be simply parametrized with  $\theta_{rms}^+$ , may suggest that modelling wall-bounded flows could reduce to modelling the dilatation at the wall, which could be studied systematically using e.g. DNS data and the evolution equation of  $\theta$  at the wall for different for different WTBCs. While this is beyond the scope of this work, the results shown here still provide an interesting physical insight, namely, that the relevant process in near-wall compressible turbulence is the level of dilatational motions, regardless of the way in which they emerge (e.g. due to changes in Mach number or boundary conditions)

The introduction of dilatational levels as a governing parameter to seek such general self-similar principles may be a promising path to collapse data not only on channels but also other wall-bounded flows across general conditions. This will require detailed well-resolved DNS studies at higher Reynolds and Mach numbers as well as a variety of boundary conditions.

**Acknowledgments.** The authors acknowledge support from the National Science Foundation (grant no. 1605914), the DoD Vannevar Bush Faculty Fellows (ONR grant no. N00014-18-1-3020), and the Extreme Science and Engineering Discovery Environment (XSEDE) for computational resources. The opinions, findings, views, conclusions and recommendations contained herein are those of the authors, and should not be interpreted as necessarily representing the official policies or endorsements, either expressed or implied, of the US Government.

**Declaration of Interests.** The authors report no conflict of interest.

| Case | $n_x$ | $n_y$ | $n_z$ | $\Delta y_{min}^+$ | $\Delta y_{max}^+$ | $\Delta x^+$ | $\Delta z^+$ | $\frac{\Delta x}{\eta} _{max}$ | $\frac{\Delta z}{\eta} _{max}$ | Marker |
|------|-------|-------|-------|--------------------|--------------------|--------------|--------------|--------------------------------|--------------------------------|--------|
| A    | 256   | 256   | 256   | 0.24               | 16.6               | 36.5         | 12.2         | 23.9                           | 7.9                            | ◁      |
| B    | 256   | 512   | 256   | 0.09               | 8.8                | 36.7         | 12.2         | 24.0                           | 8.0                            | ○      |
| C    | 512   | 512   | 512   | 0.09               | 8.8                | 18.3         | 6.1          | 12.0                           | 4.0                            | ◇      |
| D    | 640   | 512   | 512   | 0.09               | 8.8                | 14.8         | 6.1          | 9.7                            | 4.0                            | △      |
| E    | 1024  | 512   | 512   | 0.087              | 8.73               | 9.1          | 6.1          | 5.9                            | 3.94                           | □      |
| F    | 512   | 640   | 512   | 0.03               | 8.12               | 18.3         | 6.1          | 12.0                           | 3.94                           | ▷      |

Table 5. Simulation details for convergence study of an isothermal case with  $Re_\tau = 745$  and  $M_c = 2.22$ .

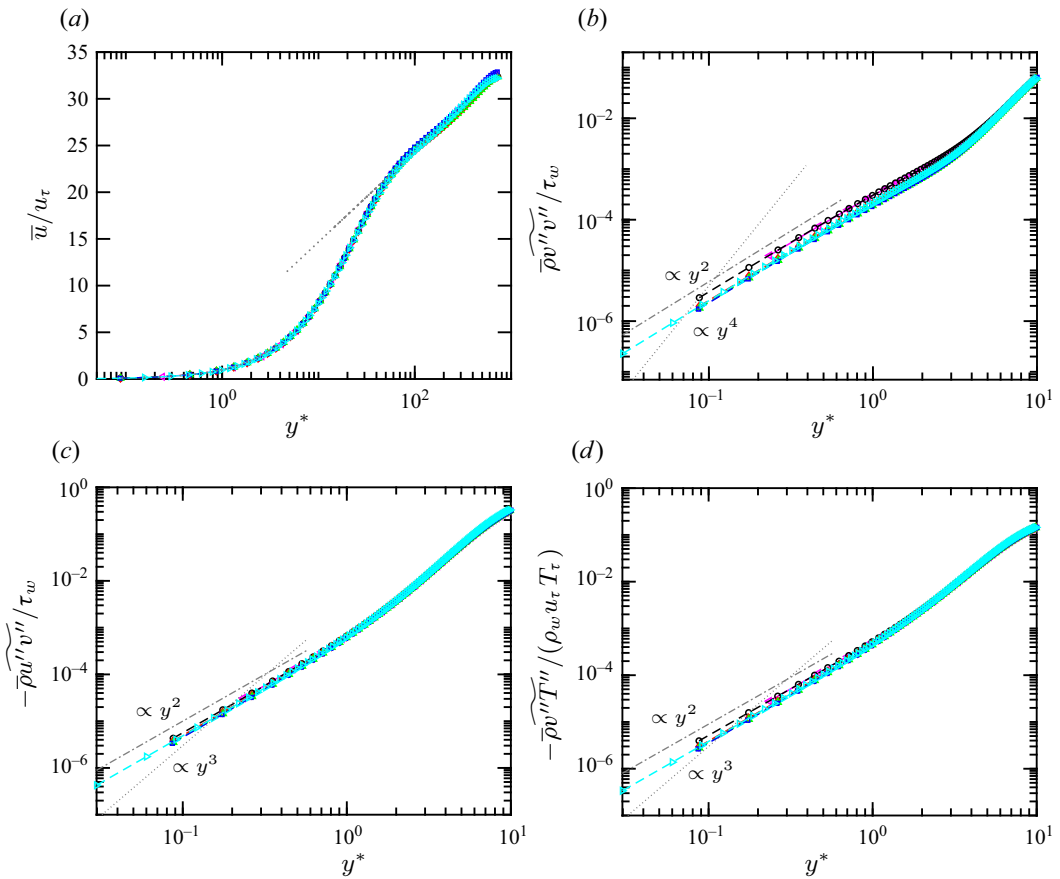


Figure 20. Grid convergence study for an isothermal case with  $Re_\tau = 745$  and  $M_c = 2.22$ . In (a), dotted grey lines correspond to viscous and log-layer scalings, for reference. In (b–d), the dotted lines correspond to the analytical solenoidal power-law scaling, and the dash-dotted lines correspond to the analytical high-speed power-law scaling as per table 2. Symbols are as in table 5.

### Appendix A

While the resolution in the wall-normal direction is higher than that commonly used, here we extend the detailed grid convergence studies of an isothermal case with  $Re_\tau = 745$  and  $M_c = 2.22$  in Baranwal *et al.* (2022), which corresponds to the most challenging condition, to assess further potential spurious numerical effects close to the wall that may

arise from inadequate grid resolution or the reduced order of the discretization close to the wall. Thus to further validate our simulations with respect to both of these potential issues, we compare simulations with different resolutions (detailed in [table 5](#)), including a new additional simulation, F in the table, with  $n_y = 640$ , which results in  $\Delta y_{min}^+ \approx 0.03$ , perhaps the highest wall-normal resolution in the literature. This provides 15 grid points in the region  $y^+ \leq 0.5$  where asymptotic scaling laws can be obtained. As seen in [figure 20](#), all qualities of interest in this work collapse for C, D, E and F close to the wall. The resolution used in this work is thus deemed appropriate.

We finally note that in general, agreement between near-wall exponents from DNS and their analytical expressions in the low and high  $M$  limits provides a power diagnostic to validate the numerical approach and assess whether the code can indeed capture the true asymptotic behaviour at the wall.

#### REFERENCES

- AGRAWAL, R., WHITMORE, M.P., GRIFFIN, K.P., BOSE, S.T. & MOIN, P. 2022 Non-Boussinesq subgrid-scale model with dynamic tensorial coefficients. *Phys. Rev. Fluids* **7** (7), 074602.
- AIKEN, T.T., BOYD, I.D., DUAN, L. & HUANG, J. 2022 Assessment of Reynolds averaged Navier–Stokes models for a hypersonic cold-wall turbulent boundary layer. In *AIAA SciTech 2022 Forum*. AIAA paper 2022-0586. AIAA.
- BAE, H.J., DAWSON, T. & MCKEON, B.J. 2020 Studying the effect of wall cooling in supersonic boundary layer flow using resolvent analysis. In *AIAA SciTech 2020 Forum*. AIAA paper 2020-0575. AIAA.
- BARANWAL, A. 2023 Mach number and thermal effects in wall-bounded compressible turbulent flows using high-resolution direct numerical simulations. *PhD thesis*, Texas A&M University.
- BARANWAL, A., DONZIS, D.A. & BOWERSOX, R.D. 2023 Turbulent heat flux in supersonic flows for different thermal boundary conditions. In *AIAA SciTech. 2023 Forum*. AIAA paper 2023-0868. AIAA.
- BARANWAL, A., DONZIS, D.A. & BOWERSOX, R.D.W. 2022 Asymptotic behaviour at the wall in compressible turbulent channels. *J. Fluid Mech.* **933**, A28.
- BLAISDELL, G.A., SPYROPOULOS, E.T. & QIN, J.H. 1996 The effect of the formulation of nonlinear terms on aliasing errors in spectral methods. *Appl. Num. Maths* **21** (3), 207–219.
- BOWERSOX, R.D.W. 2009 Extension of equilibrium turbulent heat flux models to high-speed shear flows. *J. Fluid Mech.* **633**, 61–70.
- BROSLAWSKI, C., MORREALE, B., BOWERSOX, R.D., NICHOLSON, G. & DUAN, L. 2022 Further validation and implementation of an algebraic energy flux model for high speed gaseous shear flows. In *AIAA SciTech 2022 Forum*. AIAA paper 2022-0340.
- BRUN, C., BOIARCIUC, M.P., HABERKORN, M. & COMTE, P. 2008 Large eddy simulation of compressible channel flow. *Theor. Comput. Fluid Dyn.* **22** (3–4), 189–212.
- CATRIS, S. & AUPOIX, B. 2000 Density corrections for turbulence models. *Aerosp. Sci. Technol.* **4** (1), 1–11.
- CHEN, Y. & SCALO, C. 2021 Trapped waves in supersonic and hypersonic turbulent channel flow over porous walls. *J. Fluid Mech.* **920**, A24.
- COGO, M., BAÙ, U., CHINAPPI, M., BERNARDINI, M. & PICANO, F. 2023 Assessment of heat transfer and Mach number effects on high-speed turbulent boundary layers. *J. Fluid Mech.* **974**, A10.
- COGO, M., SALVADORE, F., PICANO, F. & BERNARDINI, M. 2022 Direct numerical simulation of supersonic and hypersonic turbulent boundary layers at moderate-high Reynolds numbers and isothermal wall condition. *J. Fluid Mech.* **945**, A30.
- COLEMAN, G.N., KIM, J. & MOSER, R.D. 1995 A numerical study of turbulent supersonic isothermal-wall channel flow. *J. Fluid Mech.* **305**, 159–183.
- DONZIS, D.A. & PANICKACHERIL, J.J. 2020 Universality and scaling in homogeneous compressible turbulence. *Phys. Rev. Fluids* **5** (8), 084609.
- DUAN, L., BEEKMAN, I. & MARTIN, M.P. 2010 Direct numerical simulation of hypersonic turbulent boundary layers. Part 2 Effect of wall temperature. *J. Fluid Mech.* **655**, 419–445.
- DURBIN, P.A. 1993 A Reynolds stress model for near-wall turbulence. *J. Fluid Mech.* **249**, 465–498.
- FOYSI, H., SARKAR, S. & FRIEDRICH, R. 2004 Compressibility effects and turbulence scalings in supersonic channel flow. *J. Fluid Mech.* **509**, 207–216.
- GERMANO, M., PIOMELLI, U., MOIN, P. & CABOT, W.H. 1991 A dynamic subgrid-scale eddy viscosity model. *Phys. Fluids A* **3** (7), 1760–1765.

- GEROLYMOS, G.A. & VALLET, I. 2014 Pressure, density, temperature and entropy fluctuations in compressible turbulent plane channel flow. *J. Fluid Mech.* **757**, 701–746.
- GRIFFIN, K.P., FU, L. & MOIN, P. 2021 Velocity transformation for compressible wall-bounded turbulent flows with and without heat transfer. *Proc. Natl. Acad. Sci.* **118** (34), e2111144118.
- HADJADJ, A., BEN-NASR, O., SHADLOO, M.S. & CHAUDHURI, A. 2015 Effect of wall temperature in supersonic turbulent boundary layers: a numerical study. *Intl J. Heat Mass Transfer* **81**, 426–438.
- HUANG, J., BRETZKE, J.V. & DUAN, L. 2019 Assessment of turbulence models in a hypersonic cold-wall turbulent boundary layer. *Fluids* **4** (1), 37.
- HUANG, J., NICHOLSON, G.L., DUAN, L., CHOUDHARI, M.M. & BOWERSOX, R.D. 2020 Simulation and modeling of cold-wall hypersonic turbulent boundary layers on flat plate. In *AIAA Scitech 2020 Forum*. AIAA paper 2020-0571. AIAA.
- HUANG, P.G., COLEMAN, G.N. & BRADSHAW, P. 1995 Compressible turbulent channel flows: DNS results and modelling. *J. Fluid Mech.* **305**, 185–218.
- JAGANNATHAN, S. & DONZIS, D.A. 2016 Reynolds and Mach number scaling in solenoidally-forced compressible turbulence using high-resolution direct numerical simulations. *J. Fluid Mech.* **789**, 669–707.
- JOHN, J.P. & DONZIS, D.A. 2024 Strong evidence for universality in homogeneous compressible turbulence. *Phys. Fluids* **36** (10), 106121.
- KIDA, S. & ORSZAG, S.A. 1990 Energy and spectral dynamics in forced compressible turbulence. *J. Sci. Comput.* **5** (2), 85–125.
- LAI, Y.G. & SO, R.M.C. 1990 Near-wall modeling of turbulent heat fluxes. *Intl J. Heat Mass Transfer* **33** (7), 1429–1440.
- LI, Q., SCHLATTER, P., BRANDT, L. & HENNINGSON, D.S. 2009 DNS of a spatially developing turbulent boundary layer with passive scalar transport. *Intl J. Heat Fluid Flow* **30** (5), 916–929.
- LUSHER, D.J. & COLEMAN, G.N. 2022 Numerical study of compressible wall-bounded turbulence – the effect of thermal wall conditions on the turbulent Prandtl number in the low-supersonic regime. *Intl J. Comput. Fluid Dyn.* **36** (9), 797–815.
- MADER, T. 2000 Numerical investigation of supersonic turbulent boundary layers. *PhD thesis*, ETH Zurich.
- MENTER, F. 1992 Improved two-equation  $k-\omega$  turbulence models for aerodynamic flows. In *NASA Technical Memorandum TM-1992-103975 (NASA-TM-103975)*. NASA.
- MODESTI, D. & PIROZZOLI, S. 2016 Reynolds and Mach number effects in compressible turbulent channel flow. *Intl J. Heat Fluid Flow* **59**, 33–49.
- MORINISHI, Y., TAMANO, S. & NAKABAYASHI, K. 2004 Direct numerical simulation of compressible turbulent channel flow between adiabatic and isothermal walls. *J. Fluid Mech.* **502**, 273–308.
- PATEL, A., PEETERS, J.W.R., BOERSMA, B.J. & PECNIK, R. 2015 Semi-local scaling and turbulence modulation in variable property turbulent channel flows. *Phys. Fluids* **27** (9), 095101.
- ROY, C.J. & BLOTTNER, F.G. 2006 Review and assessment of turbulence models for hypersonic flows. *Prog. Aerosp. Sci.* **42** (7), 469–530.
- RUMSEY, C.L. 2010 Compressibility considerations for  $k-\omega$  turbulence models in hypersonic boundary-layer applications. *J. Spacecr. Rockets* **47** (1), 11–20.
- SCIACOVELLI, L., CINNELLA, P. & GLOERFELT, X. 2017 Direct numerical simulations of supersonic turbulent channel flows of dense gases. *J. Fluid Mech.* **821**, 153–199.
- SHADLOO, M.S., HADJADJ, A. & HUSSAIN, F. 2015 Statistical behavior of supersonic turbulent boundary layers with heat transfer at  $M_\infty = 2$ . *Intl J. Heat Fluid Flow* **53**, 113–134.
- SHAHAB, M.F., LEHNASCH, G., GATSKI, T.B. & COMTE, P. 2011 Statistical characteristics of an isothermal, supersonic developing boundary layer flow from DNS data. *Flow Turbul. Combust.* **86** (3–4), 369–397.
- SMITS, A.J. & DUSSAUGE, J.P. 2006 *Turbulent Shear Layers in Supersonic Flow*. Springer.
- SO, R.M.C., GATSKI, T.B. & SOMMER, T.P. 1998 Morkovin hypothesis and the modeling of wall-bounded compressible turbulent flows. *AIAA J.* **36** (9), 1583–1592.
- SO, R.M.C., LAI, Y.G., ZHANG, H.S. & HWANG, B.C. 1991a Second-order near-wall turbulence closures – a review. *AIAA J.* **29** (11), 1819–1835.
- SO, R.M.C., ZHANG, H.S. & SPEZIALE, C.G. 1991b Near-wall modeling of the dissipation rate equation. *AIAA J.* **29** (12), 2069–2076.
- SOMMER, T.P., SO, R.M.C. & ZHANG, H.S. 1993 Near-wall variable-Prandtl-number turbulence model for compressible flows. *AIAA J.* **31** (1), 27–35.
- SPALART, P. & ALLMARAS, S. 1992 A one-equation turbulence model for aerodynamic flows, In *30th Aerospace Sciences Meeting and Exhibit*. AIAA paper 92-0439. AIAA.
- TAMANO, S. & MORINISHI, Y. 2006 Effect of different thermal wall boundary conditions on compressible turbulent channel flow at  $M = 1.5$ . *J. Fluid Mech.* **548**, 361–373.

- TISELI, I., POGREBNYAK, E., LI, C., MOSYAK, A. & HETSRONI, G. 2001 Effect of wall boundary condition on scalar transfer in a fully developed turbulent flume. *Phys. Fluids* **13** (4), 1028–1039.
- TRETTEL, A. & LARSSON, J. 2016 Mean velocity scaling for compressible wall turbulence with heat transfer. *Phys. Fluids* **28** (2), 026102.
- VAN DRIEST, E.R. 1951 Turbulent boundary layer in compressible fluids. *J. Aeronaut. Sci.* **18** (3), 145–160.
- VOLPIANI, P.S., IYER, P.S., PIROZZOLI, S. & LARSSON, J. 2020 Data-driven compressibility transformation for turbulent wall layers. *Phys. Rev. Fluids* **5** (5), 052602.
- WENZEL, C., GIBIS, T. & KLOKER, M. 2022 About the influences of compressibility, heat transfer and pressure gradients in compressible turbulent boundary layers. *J. Fluid Mech.* **930**, A1.
- WENZEL, C., SELENT, B., KLOKER, M. & RIST, U. 2018 DNS of compressible turbulent boundary layers and assessment of data/scaling-law quality. *J. Fluid Mech.* **842**, 428–468.
- XU, D., WANG, J., WAN, M., YU, C., LI, X. & CHEN, S. 2021a Compressibility effect in hypersonic boundary layer with isothermal wall condition. *Phys. Rev. Fluids* **6** (5), 054609.
- XU, D., WANG, J., WAN, M., YU, C., LI, X. & CHEN, S. 2021b Effect of wall temperature on the kinetic energy transfer in a hypersonic turbulent boundary layer. *J. Fluid Mech.* **929**, A33.
- YAO, J. & HUSSAIN, F. 2020 Turbulence statistics and coherent structures in compressible channel flow. *Phys. Rev. Fluids* **5** (8), 084603.
- YU, M., XU, C. & PIROZZOLI, S. 2019 Genuine compressibility effects in wall-bounded turbulence. *Phys. Rev. Fluids* **4** (12), 123402.
- YU, M., ZHOU, Z., DONG, S., YUAN, X. & XU, C. 2024 On the generation of near-wall dilatational motions in hypersonic turbulent boundary layers. *J. Fluid Mech.* **984**, A44.
- ZHANG, C., DUAN, L. & CHOUDHARI, M.M. 2017 Effect of wall cooling on boundary-layer-induced pressure fluctuations at Mach 6. *J. Fluid Mech.* **822**, 5–30.
- ZHANG, C., DUAN, L. & CHOUDHARI, M.M. 2018 Direct numerical simulation database for supersonic and hypersonic turbulent boundary layers. *AIAA J.* **56** (11), 4297–4311.
- ZHANG, H., SO, R., SPEZIALE, C. & LAI, Y. 1992 A near-wall two-equation model for compressible turbulent flows. In *AIAA 30th Aerospace Sciences Meeting and Exhibit*. AIAA paper 92-0442. AIAA.
- ZHANG, P., SONG, Y., LIU, Y. & XIA, Z. 2022a Equivalence of three thermal boundary conditions in compressible turbulent channel flows. *Phys. Rev. E* **105** (6), 065106.
- ZHANG, P., WAN, Z., LIU, N., SUN, D. & LU, X. 2022b Wall-cooling effects on pressure fluctuations in compressible turbulent boundary layers from subsonic to hypersonic regimes. *J. Fluid Mech.* **946**, A14.
- ZHANG, Y., BI, W., HUSSAIN, F., LI, X. & SHE, Z. 2012 Mach-number-invariant mean-velocity profile of compressible turbulent boundary layers. *Phys. Rev. Lett.* **109** (5), 054502.
- ZHANG, Y., BI, W., HUSSAIN, F. & SHE, Z. 2014 A generalized Reynolds analogy for compressible wall-bounded turbulent flows. *J. Fluid Mech.* **739**, 392–420.